IQ Collaboratory III: The Empirical Dust Attenuation Framework — Taking Hydrodynamical Simulations with a Grain of Dust

ChangHoon Hahn,[1, *] Tjitske K. Starkenburg,[2] Daniel Angles-Alcázar,[3, 4] Ena Choi,[5]
Romeel Davé,[6, 7, 8] Claire Dickey,[9] Kartheik G. Iyer,[10] Ariyeh H. Maller,[11]
Rachel S. Somerville,[12, 4] Jeremy L. Tinker,[13] and L. Y. Aaron Yung[14]

[1]Department of Astrophysical Sciences, Princeton University, Peyton Hall, Princeton NJ 08544, USA
[2]Center for Interdisciplinary Exploration and Research in Astrophysics (CIERA) and
Department of Physics and Astronomy, 1800 Sherman Ave, Evanston IL 60201, USA
[3]Department of Physics, University of Connecticut, 196 Auditorium Road, U-3046, Storrs, CT 06269-3046, USA
[4]Center for Computational Astrophysics, Flatiron Institute, 162 5th Ave, New York, NY 10010, USA
[5]Quantum Universe Center, Korea Institute for Advanced Study, Hoegiro 85, Seoul 02455, Korea
[6]Institute for Astronomy, Royal Observatory, Univ. of Edinburgh, Edinburgh EH9 3HJ, UK
[7]University of the Western Cape, Bellville, Cape Town 7535, South Africa
[8]South African Astronomical Observatories, Observatory, Cape Town 7925, South Africa
[9]Department of Astronomy, Yale University, New Haven CT 06520 USA
[10]Dunlap Institute for Astronomy and Astrophysics, University of Toronto, 50 St George St, Toronto, ON M5S 3H4, Canada
[11]Department of Physics, New York City College of Technology, City University of New York, 300 Jay St., Brooklyn, NY 11201, USA
[12]Department of Physics and Astronomy, Rutgers University, 136 Frelinghuysen Road, Piscataway, NJ 08854, USA
[13]Center for Cosmology and Particle Physics, Department of Physics, New York University, 4 Washington Place, New York, NY 10003
[14]Astrophysics Science Division, NASA Goddard Space Flight Center, 8800 Greenbelt Rd, Greenbelt, MD 20771, USA

ABSTRACT

We present the Empirical Dust Attenuation (EDA) framework — a flexible prescription for assigning realistic dust attenuation to simulated galaxies based on their physical properties. Using the EDA, we forward model synthetic observations for a $M_r < -20$ complete galaxy sample for three state-of-the-art large-scale cosmological hydrodynamical simulations: SIMBA, IllustrisTNG, and EAGLE. We then compare the optical and UV color-magnitude relations, $(g-r) - M_r$ and $(FUV-NUV) - M_r$, for the forward modeled simulations to SDSS observations using likelihood-free inference. Without dust, none of the simulations can match observations as expected. With the EDA, however, we can reproduce the observed color-magnitude for all of the simulations. For SIMBA and TNG, we find an excess of luminous UV-red galaxies that dust cannot fix because they quench star formation too efficiently for the most massive galaxies. Examining the attenuation curves predicted by our dust prescription, we find good agreement with observed attenuation–slope relations and attenuation curves of star-forming galaxies. However, the EDA does not predict star-forming galaxies with low A_V since simulated star-forming galaxies are intrinsically much brighter than observations. Additionally,

the EDA provides, for the first time, predictions on the attenuation curves of quiescent galaxies, which are challenging to measure observationally. Simulated quiescent galaxies require shallower attenuation curves and lower dust attenuation than star-forming galaixes. The EDA, combined with a forward modeling, provides an effective approach for improving our understanding of dust in galaxies and probing hydrodynamical simulations. Furthermore, this work illustrates a major limitation in comparing galaxy formation models: by adjusting dust attenuation alone, simulations with significantly different galaxy populations can reproduce the same UV and optical observations.

1. INTRODUCTION

Dust in the interstellar medium of a galaxy can dramatically impact its spectral energy distribution (SED). The combined effect of dust on a galaxy's SED is typically described using an attenuation curve, $A(\lambda)$, which has now been broadly characterized by observations. In UV, attenuation curves steeply rise due to absorption by small grains. At 2175Å, in the near-UV (NUV), there is an absorption bump referred to as the "UV dust bump". At longer optical wavelengths, the curves take on a power-law shape. Finally, dust reemits the attenuated light in the optical and UV in the infrared (for an overview see Calzetti 2001; Draine 2003; Galliano et al. 2018). By impacting the SED, dust also affects the physical properties of a galaxy that are inferred from the SED, such as its star formation rate (SFR), stellar mass (M_*), or star formation history (see reviews by Walcher et al. 2011; Conroy 2013). Assumptions on dust attenuation can dramatically vary these properties (Kriek & Conroy 2013; Reddy et al. 2015; Salim et al. 2016; Salim & Narayanan 2020). Since these properties are the building blocks to our understanding of galaxies and how they evolve, a better understanding of dust not only provides insights into dust, but also underpins all galaxy studies.

To better understand dust in galaxies, many observational works have examined trends between dust attenuation and galaxy properties. For example, UV and optical attenuation are found to correlate with M_*, SFR, and metallicity in star-forming galaxies (Garn & Best 2010; Battisti et al. 2016). The slope of the attenuation curves in star-forming galaxies also correlate with galaxy properties, such as M_*, specific SFR (SSFR), metallicity, and axial ratio (Wild et al. 2011; Battisti et al. 2017). Recently, Salim et al. (2018) argue that these correlations stem from the underlying "attenuation-slope relation", a trend between the amplitude of attenuation and slope. Despite the progress, there is still no clear consensus on the connection between attenuation curves and galaxy properties. Also, studies so far have focused solely on star-forming galaxies and little is known about dust attenuation in quiescent galaxies. Furthermore, galaxy properties and dust attenuation from galaxy SEDs are model-dependent and subject to variations, inconsistencies, and biases of different methodologies, which can lead to vastly different derived results even for the same observed galaxies (*e.g.* Speagle et al. 2014; Katsianis et al. 2020). SED fitting can also impose undesirable priors on derived galaxy

* hahn.changhoon@gmail.com

properties (Carnall et al. 2018; Leja et al. 2019) and suffer from parameter degeneracies that are poorly understood.

Significant progress has also been made in theoretically modeling dust. Simulations can now model the radiative transfer of stellar light through a dusty ISM for a wide range of configurations: from simple slab-like dust geometries (*e.g.* Witt & Gordon 1996, 2000; Seon & Draine 2016) to 3D hydrodynamic simulations of entire galaxies (*e.g.* Jonsson 2006; Rocha et al. 2008; Hayward & Smith 2015; Natale et al. 2015; Hou et al. 2017). Radiative transfer models have even been applied to cosmological hydrodynamical simulations (*e.g.* Camps & Baes 2015; Narayanan et al. 2018; Trayford et al. 2020). Dust has also been examined in a cosmological context using semi-analytic models (SAMs; *e.g.* Granato et al. 2000; Fontanot et al. 2009; Wilkins et al. 2012; Gonzalez-Perez et al. 2013; Popping et al. 2017). Yet there are still major limitations in modeling dust. Dust models in cosmological simulations currently do not reproduce the redshift evolution of dust properties (Somerville et al. 2012; Yung et al. 2019; Vogelsberger et al. 2020). Also, radiative transfer models produce attenuation-slope relations that are significantly steeper than observations. Many models also require significant hand-tuning (*e.g.* propagating rays/photons into particular cells) and make assumptions on the underlying dust grain models (see Steinacker et al. 2013, for a review).

We take a different approach from the observational and theoretical works above — *we investigate dust attenuation using a forward modeling approach to compare simulations to observations*. Our "forward model" starts with three major large-scale hydrodynamical simulations: EAGLE, IllustrisTNG, and SIMBA. We use their outputs (*e.g.* star formation history) to build SEDs for each simulated galaxy. We then apply dust attenuation to all the SEDs using an Empirical Dust Attenuation framework, which we describe shortly. Finally, we apply a realistic noise model and sample selection function on the attenuated SEDs and construct synthetic photometric observations. Afterwards, we compare the synthetic observations from the forward model to actual observations. The comparisons are made in observational space, so they are not impacted by the inconsistencies of observational methods in measuring galaxy properties. Furthermore, since the forward models can directly include the selection functions and observational systematic effects, they can account for these effects to exploit the full observational data set.

An essential step in our forward model is applying the Empirical Dust Attenuation (EDA) framework, which provides a flexible and computationally inexpensive prescription for applying dust attenuation. The EDA first assigns attenuation curves to every simulated galaxy. In this work, we use the Noll et al. (2009) attenuation curve parameterization with amplitude and slope of the curves determined from the simulated galaxy's M_* and specific star formation rate (SSFR) as well as a randomly sampled inclination (i). We use the same parameterization as observational studies so that the EDA attenuation curves can easily be compared to observational constraints. The M_* and SSFR dependence is also motivated by observations (*e.g.* Garn & Best 2010; Wild et al. 2011; Battisti et al. 2016; Leja et al. 2017; Salim et al. 2018; Salim & Narayanan 2020) and allows us to easily explore the correlation between galaxy properties and dust attenuation. After the assignment, we simply apply the attenuation curves to the SEDs of the simulated galaxies. The EDA, unlike radiative transfer models, does not seek to produce realistic dust attenuation for individual galaxies.

However, as we later demonstrate, it produces realistic distributions of dust attenuation for galaxy populations. The EDA provides an empirical mapping framework for dust attenuation, analogous to the halo occupation frameworks in galaxy formation (for a review see Wechsler & Tinker 2018).

In principle, a radiative transfer model can be used instead of the EDA in the forward modeling approach; however, radiative transfer models are computationally expensive. Applying a range of radiative transfer dust models to multiple simulations for comparisons would require huge computational resources. Using them with Monte Carlo methods for parameter exploration would be prohibitive. On the other hand, with the EDA, we can apply a wide range of realistic dust attenuation to simulated galaxies in a matter of seconds. We can easily explore and sample the dust parameter space and infer the relationship between dust attenuation and galaxy properties. That is the focus of this paper. Beyond investigating dust, the EDA also provides a framework where we can treat dust as *nuisance* parameters and tractably marginalize over dust attenuation. In the subsequent paper of the IQ series, Starkenburg et al. (in preparation), we will use the EDA framework to compare star formation quenching in cosmological galaxy formation models after marginalizing over dust attenuation.

In Section 2, we describe the three large-scale cosmological hydrodynamical simulations (SIMBA, IllustrisTNG, and EAGLE) that we use in our forward model. We also describe the observed SDSS galaxy sample used for comparison. Next, we present the specific EDA prescription used in this work (Section 3) and the likelihood-free inference method for comparing the simulations to observations (Section 4). Finally, in Section 5, we present the results of our comparison and discuss their implications on dust attenuation and its connection to galaxy properties.

2. DATA

In this paper, we present the Empirical Dust Attenuation (EDA) model and demonstrate how it can be used in a forward modeling approach to compare galaxy populations in simulations and observations. For our simulations, we use three large-scale cosmological hydrodynamical simulations: the IllustrisTNG (hereafter TNG), EAGLE, and SIMBA. For our observations, we use a galaxy sample derived from SDSS. Below, we briefly describe the hydrodynamical simulations and the SDSS observations used throughout this work.

In Figure 1, we present the stellar mass functions, Φ_{M_*} left-most panel, and $M_* - $ SFR relations (right panels) of galaxies in SIMBA (orange), TNG (blue), and EAGLE (green). For reference, we include Φ_{M_*} and the $M_* - $ SFR relation for SDSS observations. For the simulations, M_* is the total stellar mass within the subhalo and SFR is the instantaneous SFR in the dense and cold star-forming gas. We do not impose any selection cuts on the simulations in Figure 1 and include both central and satellite galaxies. For SDSS, M_* is estimated using `kcorrect` (Blanton & Roweis 2007) assuming a Chabrier (2003) initial mass function and SFR is from the current release of Brinchmann et al. (2004)[1]. The uncertainties for the SDSS SMF are derived from jackknife resampling. We find striking differences between the M_*- SFR relation of SDSS and the simulations, which underscore the need for a forward modeling approach. While the M_* and SFR of simulations represent theoretical predictions,
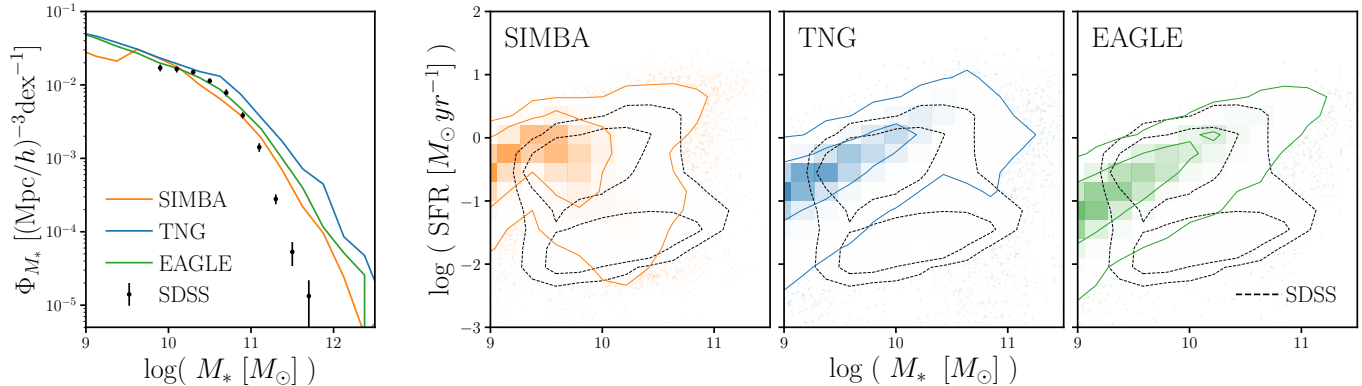
---

[1] http://www.mpa-garching.mpg.de/SDSS/DR7/

Figure 1. The stellar mass functions, Φ_{M_*} (left-most panel), and $M_* - $SFR relation (right panels) of galaxies in three cosmological hydrodynamic simulations: SIMBA (orange), TNG (blue), and EAGLE (green). For reference, we include Φ_{M_*} and the $M_* - $SFR relation of from SDSS observations (black). Uncertainties for the SDSS Φ_{M_*} are derived using jackknife resampling. We describe the simulations and observations in Section 2. There are significant differences between the $M_* - $ SFR relations of SDSS and the simulations, which are driven by the inconsistencies between the simulations' theoretical M_* and SFR predictions and the SDSS measurements. A forward modeling approach, where we construct synthetic observations for the simulations, reduces the inconsistencies and enables an apples-to-apples comparison between simulations and observation. *Furthermore, differences in Φ_{M_*} and the $M_* - $ SFR relations among the hydrodynamic simulations highlight how they predict galaxy populations with significantly different physical properties.*

the values for SDSS are subject to, for example, SFR measurement limits, inconsistencies among SFR tracers, and aperture effects. By constructing synthetic observations for the simulations with forward models, the simulations can be more consistently compared to observations (see *e.g.* Dickey et al. 2020, Starkenburg et al. in prep.) Figure 1 also illustrates that the hydrodynamical simulations predict different SMFs and $M_* - $ SFR relations from each other. This difference, which was also recently highlighted in Hahn et al. (2019c), demonstrates that *the hydrodynamical simulations predict galaxy populations with significantly different physical properties from one another*.

2.1. *IllustrisTNG100*

The IllustrisTNG100 simulation[2] is a cosmological hydrodynamic simulation of comoving volume $(110.7\,\mathrm{Mpc})^3$, with a particle mass resolution of 7.6×10^6 $M_\odot$ for dark matter and 1.4×10^6 $M_\odot$ for baryonic particles (Nelson et al. 2018; Pillepich et al. 2018; Springel et al. 2018). It improves on the original Illustris simulation[3] (Vogelsberger et al. 2014; Genel et al. 2014; public data release by Nelson et al. 2015), by including magneto-hydrodynamics and updated treatments for galactic winds, metal enrichment, and AGN feedback. Most notably, TNG uses a new implementation for feedback from SMBH, where feedback energy is injected in the form of a kinetic AGN-driven wind at low SMBH accretion rates (Weinberger et al. 2018). This new implementation has been shown to

---

[2] https://www.tng-project.org/
[3] http://www.illustris-project.org

alleviate discrepancies found between the original Illustris and observations for $> 10^{13-14} M_\odot$ massive halos.

2.2. *EAGLE*

The Virgo Consortium's EAGLE project[4] (Schaye et al. 2015; Crain et al. 2015; McAlpine et al. 2016) is a publicly available suite of cosmological hydrodynamic simulations constructed using AN-ARCHY (Dalla Vecchia et al. in prep.; see also Appendix A of Schaye et al. 2015), a modified version of the GADGET-3 code (Springel 2005). We use the L0100Ref simulation, which has a comoving volume of $(100\,\mathrm{Mpc})^3$, and a baryonic mass resolution of $1.81 \times 10^6 M_\odot$. EAGLE has subgrid models for star formation, stellar mass loss, metal enrichment and stellar feedback that stochastically inject thermal energy in the ISM as in (Dalla Vecchia & Schaye 2012). The feedback energy from AGN is also added to surrounding gas stochastically (Booth & Schaye 2009). Parameters of the stellar feedback and SMBH accretion are calibrated to broadly reproduce the $z = 0$ stellar mass function and galaxy stellar size-stellar mass relation. Meanwhile, the AGN feedback efficiency is calibrated to match the SMBH-galaxy mass relation.

2.3. *SIMBA*

The SIMBA simulation suite (Davé et al. 2019), the successor to MUFASA (Davé et al. 2016, 2017a,b), is a cosmological hydrodynamical simulation constructed using GIZMO, a meshless finite mass hydrodynamics code (Hopkins 2015; Hopkins et al. 2017). Of the suite, we use 'm100n1024', which has a box size of $(100\,h^{-1}\,\mathrm{Mpc})^3$ and baryonic mass resolution of $1.82 \times 10^7\ M_\odot$. The simulation uses some of the same subgrid models as MUFASA for H_2 based star formation, decoupled two-phase winds for star formation driven galactic winds, and feedback from Type I supernovae and AGB stars. SIMBA adds a two-mode SMBH accretion model, torque-limited accretion for cold gas (Anglés-Alcázar et al. 2017) and Bondi-based accretion for hot gas, and AGN feedback in jet, radiative, and X-ray modes.

2.4. *SDSS Galaxies*

For our observations, we use a galaxy sample derived from SDSS observations. We begin with the volume-limited Tinker et al. (2011) sample derived from the SDSS DR7 (Abazajian et al. 2009) NYU Value-Added Galaxy Catalog (VAGC; Blanton et al. 2005),which has a $M_* > 10^{9.7} M_\odot$ completeness limit. We focus on observables that can be consistently defined and derived in both simulations and observations: the r-band absolute magnitude, M_r, the optical $g-r$ color, and the $FUV-NUV$ color. We use FUV, NUV, r and g band absolute magnitudes from the NASA-Sloan Atlas[5], which is re-reduction of SDSS DR8 (Aihara et al. 2011) that includes an improved background subtraction (Blanton et al. 2011) and near and far UV photometry from GALEX. These absolute magnitudes are derived using `kcorrect` (Blanton & Roweis 2007), assuming a Chabrier (2003) initial mass function.

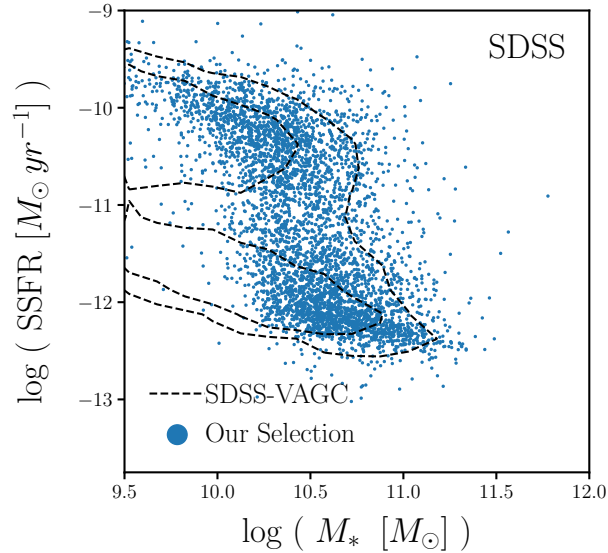[4] http://www.eaglesim.org
[5] http://nsatlas.org/

Figure 2. We derive our observational sample (blue) from the SDSS DR7 NYU-VAGC (black dashed). We impose $M_r < -20$, $M_{FUV} < -13.5$ and $M_{NUV} < -14.0$ completeness limits. We describe the galaxy sample and completess limits in more detail in Section 2.4. M_* is estimated using `kcorrect` and SSFR is from Brinchmann et al. (2004). Our SDSS sample has 4,451 galaxies that includes both star-forming and quiescent galaxies with $M_* \gtrsim 10^{10} M_\odot$.

We impose a $M_r < -20$ completeness limit on the Tinker et al. (2011) sample. We also impose completeness limits in the FUV and NUV bands. `kcorrect` UV absolute magnitudes are poorly constrained for galaxies with low UV fluxes. We compare the reconstructed FUV and NUV fluxes from `kcorrect` to the measured fluxes and determine the flux limits above which the fluxes are in good agreement. The flux limits correspond to completeness limits of $M_{FUV} < -13.5$ and $M_{NUV} < -14.0$. In Figure 2, we present the M_*-SSFR relation of our observational sample (blue). We include the original SDSS NYU-VAGC (black dash) for comparison. In total, our SDSS sample has 4,451 star-forming and quiescent galaxies with $M_* \gtrsim 10^{10} M_\odot$.

2.5. *Forward Modeling Observations*

One of the main goals of this work is to conduct an "apples-to-apples" comparison between the simulations and observations. A crucial step in this comparison is to *forward model* the observables from the simulations. The simulations can then be directly compared to observations in observational-space. Then the comparison does not rely on measured galaxy properties, which are impacted by variations, inconsistencies, and biases of different methods (Dickey et al. 2020). The comparison can also include selection functions and observational systematic effects through the forward model. In this work, we use r-band luminosity (M_r), optical color ($g-r$), and UV color ($FUV-NUV$) as our observables.

As the first step in our forward model, we construct SEDs for all of the simulated galaxies based on their star formation and metallicity histories (SFH and ZH) using the Flexible Stellar Population Synthesis model (`FSPS`; Conroy et al. 2009, 2010) with the MILES spectral library (Sánchez-Blázquez

et al. 2006) and MIST isochrones (Paxton et al. 2011, 2013, 2015; Choi et al. 2016; Dotter 2016). For each simulated galaxy, we bin the total stellar mass formed by age (t) and metallicity (Z). We use the same t, Z grid for all of the simulations to account for the variable time and mass resolutions. For each point in the t, Z grid, we generate a spectrum assuming a simple stellar population (SSP) using FSPS and take the mass-weighted linear combination of them to produce the galaxy SED. We use a Chabrier (2003) initial mass function. For further details on how we construct the SEDs, we refer readers to Starkenberg et al. (in prep.).

Next, we apply dust attenuation to the SEDs. We use the EDA prescription to assign dust attenuation curves for each simulated galaxy based on its physical properties, a randomly sampled inclination, and EDA model parameters. We describe the EDA framework in detail later in Section 3. We measure the observables by convolving the attenuated SEDs with transmission curves of the GALEX FUV, GALEX NUV, SDSS g, and SDSS r broadband filters. We add realistic noise to M_r, $g-r$, and $FUV-NUV$ by sampling from the observed uncertainty distributions of the NASA Sloan-Atlas. Lastly, we apply the $M_r < -20$, $M_{FUV} < -13.5$, and $M_{NUV} < -14$ absolute magnitude completeness limits of our SDSS sample to the simulated galaxies.

In Figure 3, we present the forward modeled optical and UV color-magnitude relations, $(g-r)-M_r$ (top) and $(FUV-NUV) - M_r$ (bottom), for simulated galaxies in SIMBA (left), TNG (center) and EAGLE (right) *assuming no dust attenuation*. We mark the 68 and 95% contours and include, for reference, the optical and UV color-magnitude relations of our SDSS sample (black dashed). Comparison to SDSS observations clearly demonstrate that *without dust attenuation, the hydrodynamical simulations do not reproduce the observed optical or UV color-magnitude relations.*

3. THE EMPIRICAL DUST ATTENUATION FRAMEWORK

In this section, we describe the Empirical Dust Attenuation (EDA) framework and present the EDA prescription we use in this work. The EDA is a flexible framework for applying dust attenuation curves to simulated galaxy populations. For each simulated galaxy, the EDA assigns a dust attenuation curve that is parameterized as a function of the galaxy's properties (M_*, SSFR), the EDA parameters, and randomly sampled inclination. With the EDA, we can apply a wide variety of dust attenuation that include correlation between dust attenuation and physical galaxy properties.

We begin by defining the dust attenuation curve, $A(\lambda)$, as

$$F_o(\lambda) = F_i(\lambda)10^{-0.4A(\lambda)} \tag{1}$$

where F_o is the observed flux and F_i is the intrinsic flux. We normalize the attenuation to the V band attenuation,

$$A(\lambda) = A_V \frac{k(\lambda)}{k_V} \tag{2}$$

so that A_V determines the amplitude of the attenuation, while $k(\lambda)$ determines the wavelength dependence.

The EDA framework assigns $A(\lambda)$ to every galaxy in the simulations using some flexible prescription. For the EDA prescription in this work, we assign A_V for each galaxy using the slab model,
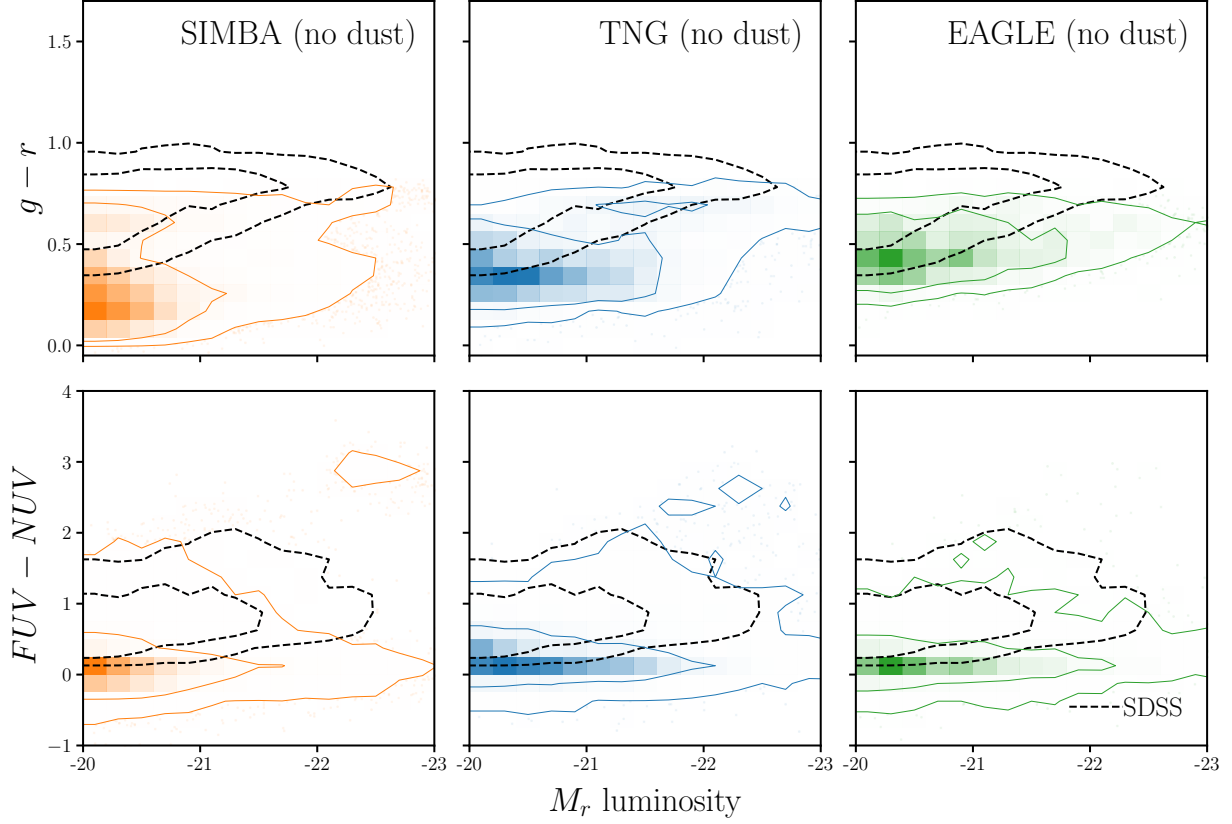
Figure 3. We present the forward modeled optical and UV color-magnitude relations of SIMBA (left), TNG (center), and EAGLE (right) galaxies *assuming no dust attenuation*. We present $(g−r) − M_r$ in the top panels and $(FUV−NUV) − M_r$ in the bottom panels. The contours represent the 68 and 95% of the distribution. We derive observables M_r, $g−r$, and $FUV−NUV$ for the simulations using our forward model (Section 2.5). For comparison, we include the color-magnitude relations of our SDSS sample (black dashed; Section 2.4). *Without dust attenuation, the hydrodynamical simulations do not reproduce the SDSS optical or UV color-magnitude relations.*

where A_V is a function of galaxy inclination, i, and its optical depth, τ_V (*e.g.* Somerville & Primack 1999; Somerville et al. 2012):

$$A_V = -2.5 \log \left[\frac{1 - e^{-\tau_V \, \sec i}}{\tau_V \, \sec i} \right]. \tag{3}$$

We parameterize τ_V using a linear M_* and SSFR dependence:

$$\tau_V(M_*, \text{SFR}) = m_{\tau, M_*} \log \left(\frac{M_*}{10^{10} M_\odot} \right) + m_{\tau, \text{SSFR}} \log \left(\frac{\text{SSFR}}{10^{-10} yr^{-1}} \right) + c_\tau. \tag{4}$$

m_{τ, M_*}, $m_{\tau, \text{SSFR}}$, and c_τ represent the M_* dependence, the SSFR dependence, and amplitude of τ_V. Since τ_V is optical depth, we impose a $\tau_V \geq 0$ limit. For each galaxy, we uniformly sample $\cos i$ from 0 to 1. By sampling $\cos i$, our EDA prescription includes significant variance in $A(\lambda)$ so galaxies with the same galaxy properties do not have the same dust attenuation.

Previous works have parameterized dust attenuation based on galaxy properties such as its gas density, gas metallicity, or star-gas geometry, motivated by the fact that dust on small scales depend

on local stellar and gas properties (*e.g.* Somerville & Primack 1999; Somerville et al. 2012; Steinacker et al. 2013; Camps & Baes 2015; Narayanan et al. 2018; Trayford et al. 2020; Vogelsberger et al. 2020). The galaxies in the SIMBA, TNG, and EAGLE simulations, however, have substantially different gas masses and metallicites (Davé et al. 2020, Maller *et al.* in prep.). If we were to parameterize τ_V using these properties, the differences in them between the simulations would dominate any comparison of dust attenuation. Instead, our parameterization for τ_V is based on the correlation between dust attenuation and galaxy properties that have been established by observations (*e.g.* Garn & Best 2010; Battisti et al. 2016; Salim & Narayanan 2020). In Appendix A, we confirm the correlation between A_V and the properties M_* and SSFR using the Salim et al. (2018) GSWLC2 sample (Figure 14). We therefore include in Eq. 4 the correlation between A_V and galaxy M_* and SSFR.

In Eq. 3, we use the slab model because it provides a simple prescription for generating a distribution of A_V that depends on randomly sampled i, with loose physical motivations. For star-forming galaxies, which typically have disc-like morphologies, the slab model produces A_V that is correlated with i in a way consistent with observations: edge-on galaxies have higher A_V than face-on galaxies (*e.g.* Conroy et al. 2010; Wild et al. 2011; Battisti et al. 2017; Salim & Narayanan 2020). Nevertheless, the slab model is a simplification. In reality, A_V depends on the detailed star-to-dust geometry. Furthermore, all galaxies, not just star-forming, in the simulations are assigned A_V from the slab model. For quiescent galaxies, which typically have elliptical morphologies, the slab model serves only as an *empirical* prescription for statistically sampling A_V. However, the purpose of the EDA is to assign an accurate distribution of dust attenuation curves for the galaxy population — *not* to accurately model dust attenuation for individual galaxies. In this regard, we demonstrate that the slab model based EDA can match the observed distribution of A_V, even for samples that include quiescent galaxies (Appendix A). Hence, the slab model provides a sufficient prescription for reproducing the A_V distribution for an ensemble of galaxies.

For the wavelength dependence of the attenuation curve, $k(\lambda)$, we use Noll et al. (2009):

$$k(\lambda) = (k_{\rm Cal}(\lambda) + D(\lambda)) \left(\frac{\lambda}{\lambda_V} \right)^{\delta}. \tag{5}$$

Here $k_{\rm Cal}(\lambda)$ is the Calzetti (2001) curve:

$$k_{\rm Cal}(\lambda) = \begin{cases} 2.659(-1.857 + 1.040/\lambda) + R_V, & 6300A \leq \lambda \leq 22000A \\ 2.659(-2.156 + 1.509/\lambda - 0.198/\lambda^2 + 0.011/\lambda^3) + R_V & 1200A \leq \lambda \leq 6300A \end{cases}$$

where $\lambda_V = 5500A$ is the V band wavelength and δ is the slope offset of the attenuation curve from $k_{\rm Cal}$. Since δ correlates with galaxy properties (*e.g.* Wild et al. 2011; Battisti et al. 2016; Leja et al. 2017; Salim et al. 2018, ; see also Appendix A), we parameterize δ with a similar M_* and SSFR dependence as τ_V:

$$\delta(M_*, {\rm SFR}) = m_{\delta,M_*} \log \left(\frac{M_*}{10^{10} M_\odot} \right) + m_{\delta,{\rm SFR}} \log \left(\frac{\rm SSFR}{10^{-10} yr^{-1}} \right) + c_\delta. \tag{6}$$

$D(\lambda)$ in Eq. 5 is the UV dust bump, which we parameterize using the standard Lorentzian-like Drude profile:

$$D(\lambda) = \frac{E_b(\lambda \ \Delta\lambda)^2}{(\lambda^2 - \lambda_0^2)^2 + (\lambda \ \Delta\lambda)^2} \tag{7}$$

where λ_0, $\Delta\lambda$, and E_b are the central wavelength, full width at half maximum, and strength of the bump, respectively. We include the UV dust bump since we use UV color as one of our observables. We assume fixed $\lambda_0 = 2175A$ and $\Delta\lambda = 350A$. Kriek & Conroy (2013) and Tress et al. (2018) find that E_b correlates with the δ for star-forming galaxies $z \sim 2$. Narayanan et al. (2018) confirmed this dependence in simulations. We assume a fixed relation between E_B and δ from Kriek & Conroy (2013): $E_b = -1.9 \ \delta + 0.85$. Allowing the slope and amplitude of the E_B and δ relation to vary does *not* impact our results; however, we also do not derive any meaningful constraints on them. In Table 1, we list and describe all of the free parameters of our EDA prescription.

SSFR of galaxies are used to calculate τ_V and δ in Eqs. 4 and 6. However, due to mass and temporal resolutions, some galaxies in the simulations have SFR $= 0$ — *i.e.* an unmeasurably low SFR (Hahn et al. 2019c). They account for 17, 19, 9% of galaxies in SIMBA, TNG, and EAGLE, respectively. Since Eqs. 4 and 6 depend on $\log$ SSFR, they cannot be used in the equations to derive τ_V and δ for these galaxies. To account for this issue, we assign SFR$_{\min}$, the minimum non-zero SFR in the simulations, to SFR $= 0$ galaxies when calculating τ_V and δ. For SIMBA, TNG, and EAGLE, SFR$_{\min} = 0.000816, 0.000268$, and $0.000707 M_\odot/yr$, respectively. Although this assumes that SFR $= 0$ galaxies have similar dust properties as the galaxies with SFR $=$ SFR$_{\min}$, since the simulations have very low SFR$_{\min}$ we expect galaxies with SFR $=$ SFR$_{\min}$ to have little recent star-formation and low gas mass, similar to SFR $= 0$ galaxies.

In practice, to apply the EDA to a simulated galaxy population, we first assign a randomly sampled i to each galaxy ($\cos i$ uniformly sampled from 0 to 1). τ_V and δ are calculated for the galaxy based on its M_*, SSFR and the EDA parameters. We then combine A_V from i and τ_V with $k(\lambda)$ from δ to determine $A(\lambda)$ for each galaxy. Afterwards, we attenuate the galaxy SEDs using Eq. 1 and use the attenuated SEDs to calculate the observables: g, r, NUV, and FUV absolute magnitudes. In Figure 4, we present attenuation curves, $A(\lambda)$, generated by the EDA for galaxies with different SFR and M_* values. We include star-forming galaxies with $\{M_*, \text{SFR}\} = \{10^{10} M_\odot, 10^{0.5} M_\odot/yr\}$ (blue), $\{10^{11} M_\odot, 10^1 M_\odot/yr\}$ (green) and a quiescent galaxy with $\{10^{11} M_\odot, 10^{-2} M_\odot/yr\}$ (red). We use an arbitrarily set of EDA parameters $(m_{\tau,M_*}, m_{\tau,\text{SSFR}}, c_\tau, m_{\delta,M_*}, m_{\delta,\text{SFR}}, c_\delta)$ within the prior range listed in Table 1. We set $i = 0$ (edge-on) for all $A(\lambda)$ in Figure 4 for simplicity. For comparison, we include the Calzetti (2001) attenuation curve. Even when we set $i = 0$, the EDA produces attenuation curves with a wide range of amplitude and slope to galaxies based on their physical properties.

4. LIKELIHOOD-FREE INFERENCE: APPROXIMATE BAYESIAN COMPUTATION

With our forward model, which includes the EDA prescription for dust attenuation, we can now generate synthetic observations for simulated galaxies and make an "apples-to-apples" comparison to SDSS. Next, we want to use this comparison to infer the posterior probability distribution of the EDA parameters. Typically in astronomy, this inference is done assuming a Gaussian likelihood to compare the "summary statistic" (*e.g.* SMF) of the model to observations and some sampling
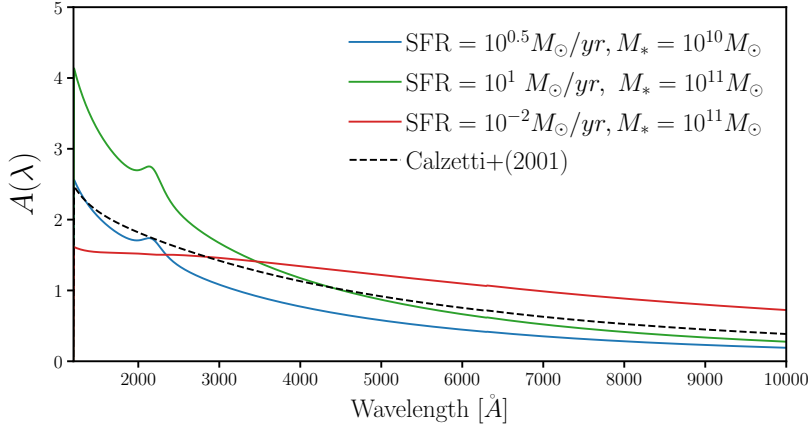
Figure 4. Attenuation curves, $A(\lambda)$, assigned by our Empirical Dust Attenuation (EDA) prescription to edge-on galaxies with different SFR and M_* values for an arbitrary set of EDA parameters. We include $A(\lambda)$ for star-forming galaxies with $\{M_*, \text{SFR}\} = \{10^{10}M_\odot, 10^{0.5}M_\odot/yr\}$ (blue), $\{10^{11}M_\odot, 10^1 M_\odot/yr\}$ (green) and a quiescent galaxy with $\{10^{11}M_\odot, 10^{-2}M_\odot/yr\}$ (red). We set $i = 0$ for all the galaxies in the figure for simplicity but in practice the EDA uniformly samples $\cos i$ from 0 to 1 for each galaxy. For comparison, we include the Calzetti (2001) attenuation curve. *The EDA provides a flexible prescription for assigning dust attenuation to galaxies based on their inclination, physical properties (M_* and SSFR), and the EDA parameters.*

Table 1. Free parameters of the Empirical Dust Attenuation Model

Parameter	Definition	prior
m_{τ,M_*}	M_* dependence of the optical depth, τ_V	flat $[-5., 5.]$
$m_{\tau,\text{SSFR}}$	SSFR dependence of τ_V	flat $[-5., 5.]$
c_τ	amplitude of τ_V	flat $[0., 6.]$
m_{δ,M_*}	M_* dependence of δ, the attenuation curve slope offset	flat $[-4., 4.]$
$m_{\delta,\text{SFR}}$	SSFR dependence of δ	flat $[-4., 4.]$
c_δ	amplitude of δ	flat $[-4., 4.]$

method (*e.g.* Markov Chain Monte Carlo) to estimate the posterior distribution. The functional form of the likelihood, however, depends on the summary statistic and assuming an incorrect form of the likelihood can significantly bias the inferred posteriors (*e.g.* Hahn et al. 2019b). In this work, we use the optical and UV color-magnitude relations as our summary statistic. Since this statistic is a three-dimensional histogram, the likelihood is *not* Gaussian. Furthermore, since the bins are not independent the true likelihood is difficult to analytically write down.

Rather than *incorrectly* assuming a Gaussian likelihood or attempting to estimate the true likelihood of the optical and UV color-magnitude relations, we use Approximate Bayesian Computation (hereafter ABC; Diggle & Gratton 1984; Tavare et al. 1997; Pritchard et al. 1999; Beaumont et al. 2009; Del Moral et al. 2012) for our inference. ABC is a likelihood-free (or "simulation-based")

parameter inference framework that approximates the posterior probability distribution, $p(\theta \,|\, \text{data})$, without requiring evaluations of the likelihood. Instead, ABC only requires a forward model of the observed data, a prior that can be sampled, and a distance metric that quantifies the "closeness" to the observed data. Since ABC does not require evaluating the likelihood, it does not assume any functional form of the likelihood so we avoid any biases from such assumptions. It also expands the summary statistics we can use to infer the posteriors. ABC, therefore, provides a general inference framework for our forward modeling approach (Hahn et al. 2017a).

In the simplest version of ABC, with a rejection sample framework (Pritchard et al. 1999), a proposal set of parameter values are drawn from the prior. The forward model is run with the proposal parameter values. The output of the forward model is then compared to the observed data using a distance metric that quantifies the "closeness" of the forward model output to the observed data. If the distance is within some small threshold, we keep the proposed parameters; otherwise, we discard them. Proposals are drawn until enough pass the threshold to sample the posterior. A rejection sampling framework requires a large number of evaluations of the forward model, which can be computationally costly. Many variations of ABC with more efficient sampling strategies have now been applied to astronomy and cosmology (*e.g.* Cameron & Pettitt 2012; Weyant et al. 2013; Ishida et al. 2015; Lin et al. 2016; Alsing et al. 2018). Among these methods, we use ABC with Population Monte Carlo (PMC) importance sampling (Hahn et al. 2017a,b, 2019a).

ABC-PMC begins with an arbitrarily large threshold ϵ_1 and N proposals $\bar{\theta}_1$ sampled from the prior distribution. Each proposal is assigned a weight $w_1^i = 1/N$. Then for subsequent iterations ($n > 1$), the threshold, ϵ_n, is set to the median distance of the previous iteration's proposals. New proposals are drawn from the previous iteration's proposals perturbed by a kernel and kept if their distance is below ϵ_n. This is repeated until we assemble a new set of N proposals $\bar{\theta}_n$. The entire process is repeated for the next iteration until convergence is confirmed. We use the Python implementation of Akeret et al. (2015)[6]. For further details on the ABC-PMC implementation, we refer readers to Hahn et al. (2017b) and Hahn et al. (2019a).

In this work, we use ABC-PMC with uninformative uniform priors on each of the EDA parameters and choose ranges that encompass constraints in the literature. The prior ranges of $m_{\tau,M_*}, m_{\tau,\text{SSFR}}, c_\tau$ include the A_V range and M_* and SFR dependence of Narayanan et al. (2018) and Salim & Narayanan (2020). Meanwhile, the prior ranges of $m_{\delta,M_*}, m_{\delta,\text{SFR}}, c_\delta$ include the δ range and M_* and SFR dependence of Leja et al. (2017) and Salim et al. (2018). We list the range of the priors in Table 1. For our forward model, we use the model described in Section 2.5: we construct SEDs for every simulated galaxy from the hydrodynamic simulations, apply dust attenuation with our EDA, calculate the observables (M_r, $g-r$, and $FUV-NUV$), apply a noise model to them, and apply a $M_r < -20$ completeness limit. We use the optical and UV color-magnitude relation, $(g-r) - M_r$ and $(FUV-NUV) - M_r$ as our summary statistic to fully exploit the $(M_r, g-r, FUV-NUV)$ observational-space. We measure the color-magnitude relations by calculating the number density in bins of $(g-r, FUV-NUV, M_r)$ with widths $(0.0625, 0.25, 0.5)$ $mags$. For our distance metric, ρ, we use the L2 norm between the

---

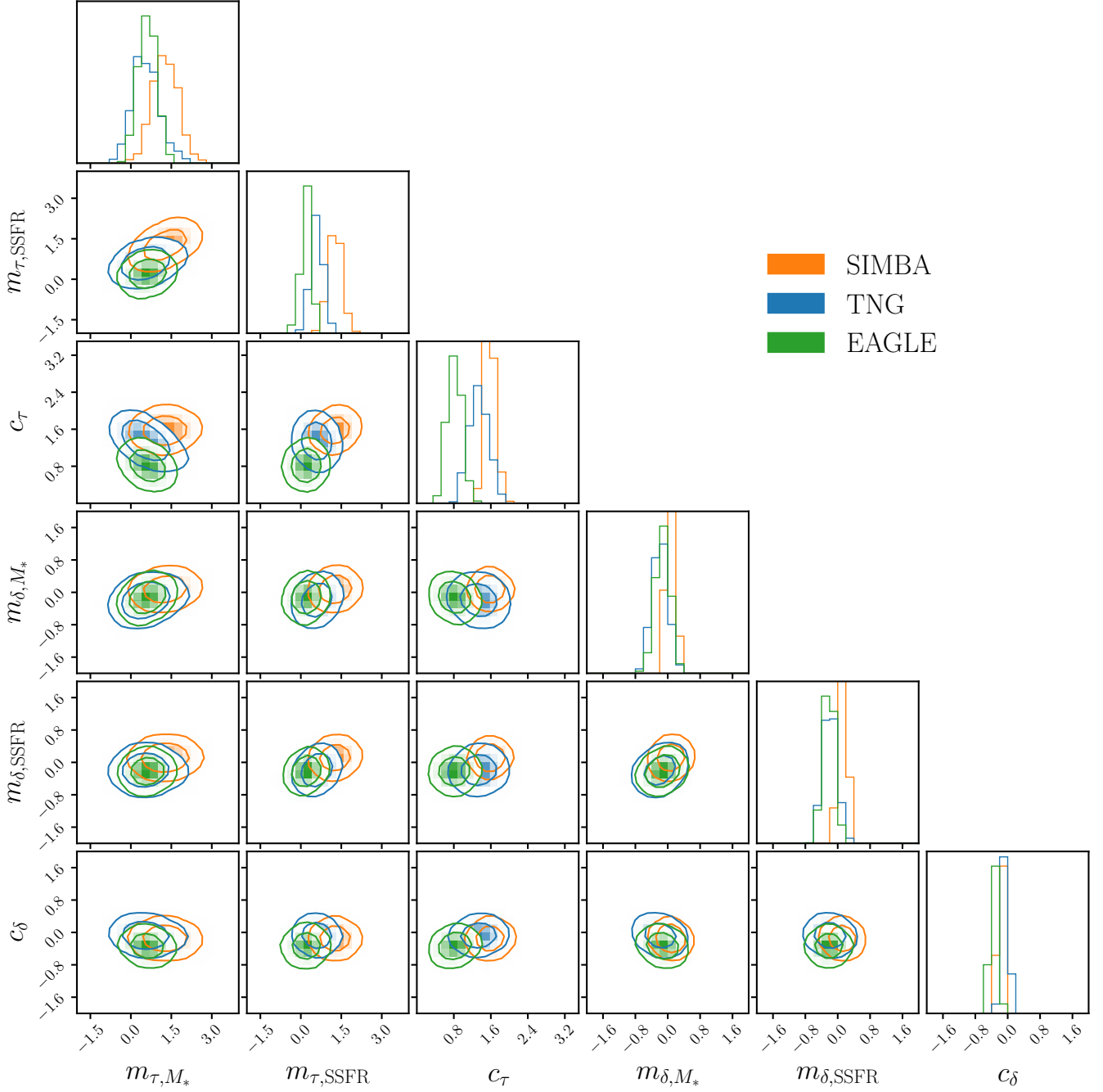[6] https://abcpmc.readthedocs.io/en/latest/index.html

Figure 5. Posterior distributions of the EDA parameters for the SIMBA (orange), TNG (blue), and EA-GLE (green) hydrodynamical simulations. The contours mark the 68 and 95 percentiles of the distributions. The posteriors are derived from likelihood-free inference using Approximate Bayesian Computation with Population Monte Carlo (Section 4).

number density of the SDSS observation, n^{SDSS} and of our forward model, $n^{\mathrm{FM}}(\theta_{\mathrm{EDA}})$:

$$\rho(\theta_{\mathrm{EDA}}) = \sum_{i,j} \left[n_{ij}^{\mathrm{SDSS}} - n_{ij}^{\mathrm{FM}}(\theta_{\mathrm{EDA}}) \right]^2 . \tag{8}$$
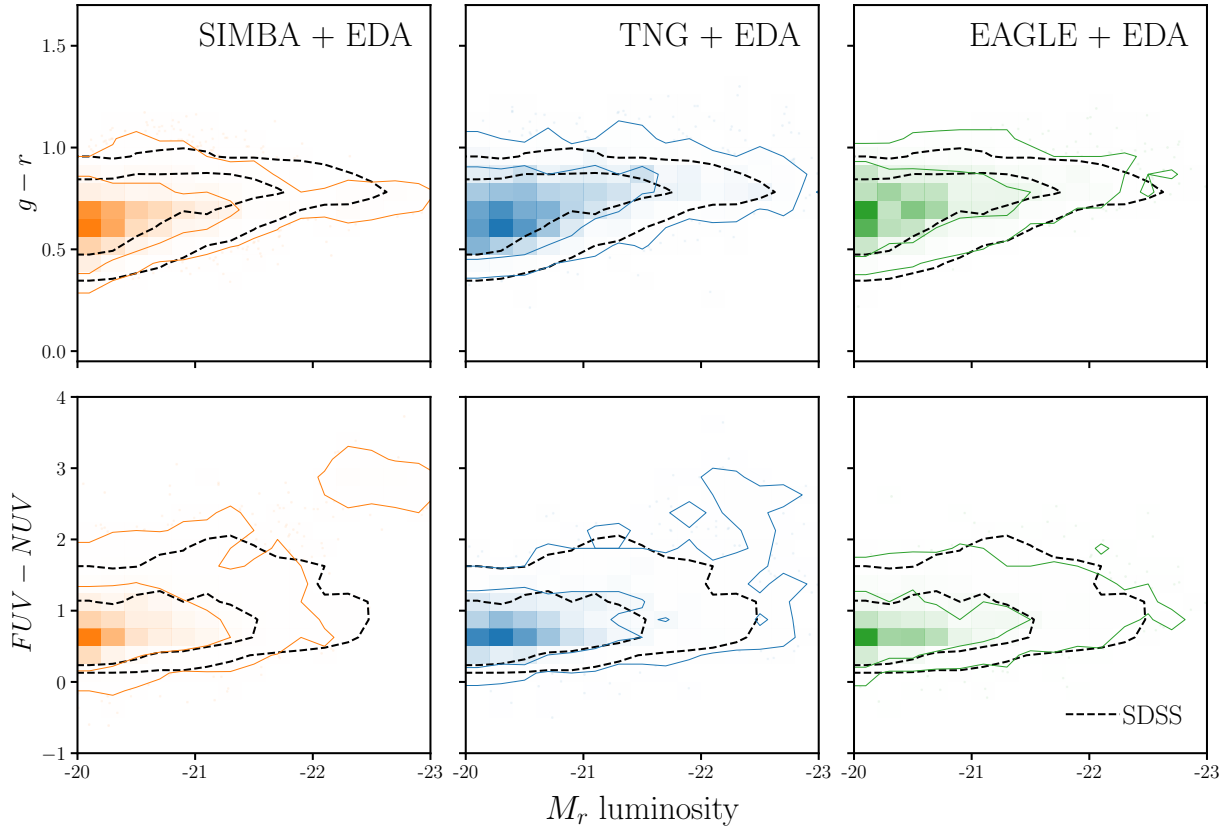
Figure 6. The optical, $(g-r)-M_r$ (top), and UV, $(FUV-NUV)-M_r$ (bottom), color-magnitude relations predicted by our EDA prescription for the SIMBA (orange), TNG (blue), and EAGLE (green) hydrodynamical simulations. For the EDA parameters of each simulation, we use the median of the posterior distributions inferred using ABC. For comparison, we include the color-magnitude relations of SDSS (black dashed). Comparing the color-magnitude relations above to those without dust attenuation in Figure 3, we see that dust *dramatically* impacts the color-magnitude relations. Dust attenuation must be accounted for when interpreting and comparing simulations. Furthermore, with our EDA prescription, all three simulations reproduce the color-magnitude relations of SDSS observations. *Since the different simulations can reproduce observations just by varying dust, dust significantly limits our ability to constrain the underlying physical processes of galaxy formation models.*

In Figure 5, we present the posterior distributions of the EDA parameters derived using ABC-PMC for the SIMBA (orange), TNG (blue), and EAGLE (green) hydrodynamical simulations. The contours mark the 68 and 95 percentiles of the distributions.

5. RESULTS

Without dust attenuation, all of the hydrodynamical simulations struggle to reproduce the $(g-r) - M_r$ and $(FUV-NUV) - M_r$ relations of SDSS (Figure 3). Both in the optical and UV, the simulations predict galaxies with significantly bluer than SDSS galaxies. The simulations also predict optically blue luminous galaxies with $M_r < -21.5$ that are not found in the observations; this is particularly noticeable for SIMBA and TNG. Simulated galaxies in SIMBA also have a sig-

nificantly broader distribution of $g-r$ colors than SDSS galaxies. Meanwhile, all of the simulations predict a broader distribution of $FUV-NUV$ color than SDSS. In fact, SIMBA and TNG predict a significant number of luminous galaxies, $M_r < -22$, with $FUV-NUV > 2$ colors, which extends beyond SDSS observations.

With our EDA prescription, all three simulations produce color-magnitude relations that are highly consistent with SDSS observations. In Figure 6, we present the optical and UV color-magnitude relations predicted by the EDA for the SIMBA (orange), TNG (blue), and EAGLE (green) simulations. For the EDA parameters, we use the median of the inferred posterior distributions (Figure 5). We include the color-magnitude relations of SDSS observations (black-dashed) comparison. The contours mark the 68 and 95 percentiles of the distributions.

Dust dramatically impacts the observables of simulations. The EDA affects the the optical and UV color-magnitude relations in three major ways to produce good agreement with SDSS. First, the EDA significantly reddens the simulated galaxies in the optical: $g-r$ colors are $\gtrsim 0.25\ mag$ redder than the optical color-magnitude relation in Figure 3 and match the $g-r$ distribution of SDSS. Second, the EDA significantly reddens non-quiescent ($\log \mathrm{SSFR} > -11$) galaxies in the UV. While quiescent galaxies have intrinsically red UV colors, $FUV-NUV > 0.5$, that generally agree with SDSS, the rest of the galaxies are intrinsically bluer in the UV than observations. The EDA reddens their $FUV-NUV$ colors by $\gtrsim 0.5\ mag$. Lastly, the EDA also attenuates non-quiescent galaxies. As a result, there are no longer luminous galaxies that are blue in the optical or UV — consistent with observations.

Despite the substantial improvement in the color-magnitude relation agreement with the EDA, there is still one significant discrepancy: the presence of luminous $M_r > -22$ galaxies that are UV-red $FUV-NUV > 2$, not found in observations. This galaxy population, which consists of quiescent galaxies with SFR $\lesssim 10^{-2} M_\odot/yr$, is especially pronounced in the UV color-magnitude of SIMBA but also present in TNG. They are also present in the UV color-magnitude predictions without dust attenuation (Figure 3). Since these galaxies are luminous and they have intrinsic $FUV-NUV > 2$, dust attenuation cannot remove them from the UV color-magnitude relation. In other words, the excess luminous UV-red galaxies predicted by SIMBA and TNG are irreconcilable even with dust attenuation.

In order to understand the origin of the luminous UV-red galaxies in SIMBA (left) and TNG (right), we examine their star formation histories in Figure 7. The top and center panels mark the luminous UV-red galaxies on the optical and UV color-magnitude relations predicted by the EDA (red). The bottom panels present the median specific SFH (SSFH), SSFR as a function of lookback time, t_{lookback}, with the shaded regions representing the 68 percentile of the SSFH. For comparison, we include the SSFHs of other quiescent galaxies (SSFR $< 10^{-11} yr^{-1}$) with matching luminosities, $M_r < -22$ (orange). The SSFHs reveal that, unlike other quiescent galaxies, the luminous UV-red galaxies of SIMBA and TNG have almost no star formation within the last $t_{\mathrm{lookback}} \lesssim 2$ Gyr. With no recent star formation contributing to the SED in FUV wavelength, these galaxies have faint FUV magnitudes and, thus, high $FUV-NUV$ color. The luminous UV-red galaxies in SIMBA and TNG,
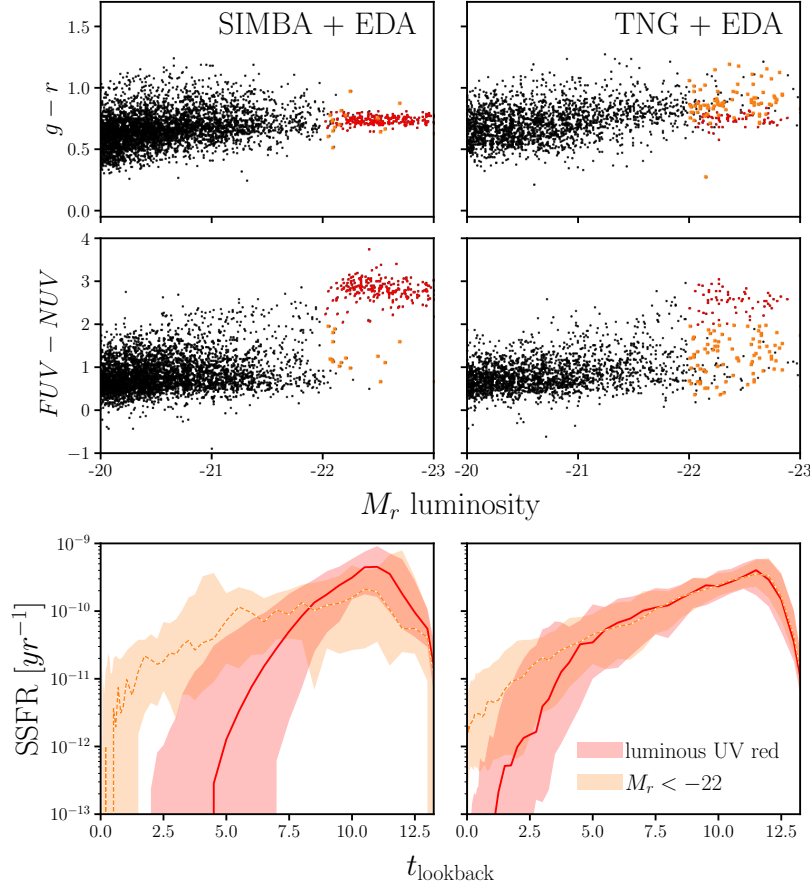
Figure 7. The SFHs of luminous UV red galaxies (red) in SIMBA (left) and TNG (right) that cause the discrepancy between the color-magnitude relations predicted by the EDA and SDSS observations. We include the SFHs of quiescent galaxies with matching luminosities, $M_r < -22$, for comparison (orange). The top and center panels mark the luminous UV red and the other $M_r < -22$ galaxies in the EDA predicted optical and UV color-magnitude relations, respectively. In the bottom panels, we present the median SSFH of these galaxies with the shaded regions representing the 68 percentiles of the SSFH. In both TNG and SIMBA, the luminous UV red galaxies have negligible star formation within the last 2 Gyrs, unlike the other quiescent galaxies. *Therefore, SIMBA and TNG pedict luminous UV red galaxies not found in observations because their prescription for star formation quenching is too efficient in the most massive galaxies.*

which are not found in observations, are a consequence of star formation quenching being too efficient in the most massive quiescent galaxies.

The SSFHs in Figure 7 also reveal that luminous UV-red galaxies in SIMBA have a substantially different SSFH than other quiescent galaxies. Besides, the lack of recent star formation, the luminous UV-red galaxies also have significantly shorter star-forming timescales. They peak their star formation earlier than other quiescent galaxies at $t_{\rm lookback} \sim 11$ Gyr and have a more rapid decline in star formation. In contrast, the luminous UV-red galaxies in TNG have overall similar SSFHs to other quiescent galaxies. This difference in SFH suggests that a distinct star formation quenching mechanism is responsible for the luminous red galaxies in SIMBA. In another paper of the IQ series

18

(Choi et al. in prep), we examine this SFH difference in further detail and present its impact on the quiescent fraction evolution over $0 < z < 3$.

In principle, the simulations could also remove the luminous UV-red galaxies from the sample if star formation quenching in these galaxies was *even* more efficient. With absolutley no recent star formation, their UV SED would fall below our magnitude limit and would not be included in the comparison. However, a large portion of the luminous quiescent galaxies are luminous UV-red galaxies, so the simulations, especially SIMBA, would struggle to reproduce the luminous tip of the SDSS red sequence. Furthermore, reducing the total number of massive quiescent galaxies that pass the selection function would conflict with our observations, which includes a significant number of massive quiescent galaxies (Figure 2).

Previous works in the literature have also compared simulations with different dust prescriptions to observations in color-magnitude space. For EAGLE, Trayford et al. (2015) calculate colors and luminosities with the GALAXEV population synthesis models and a two-component screen model for dust. More recently, Trayford et al. (2017) calculated optical colors for EAGLE using SKIRT, a Monte Carlo radiative transfer code (Camps & Baes 2015), to model the dust. At stellar masses and luminosities comparable to our SDSS sample, both Trayford et al. (2015) and Trayford et al. (2017) produce red sequences bluer than in GAMA observations. Also, Trayford et al. (2015) predict an excess of luminous blue galaxies. Although a detailed comparison is difficult since both works compare to different observations, we note that with the EDA, EAGLE is able to successfully reproduce the position of the SDSS red sequence and does not predict a significant excess of luminous blue galaxies. Also using EAGLE and SKIRT, Baes et al. (2019) find that they overestimate the observed cosmic SED (CSED) in the UV regime and produce significantly higher $FUV-NUV$ color than GAMA. The EDA for EAGLE predict $FUV-NUV$ in good agreement with SDSS. For TNG, Nelson et al. (2018) calculate optical colors using a dust model that includes attenuation due to dense gas birth clouds surrounding young stellar populations and also due to simulated distribution of neutral gas and metals. They find bluer red sequence peaks and a narrower blue cloud compared to SDSS. We find neither of these discrepancies for the TNG+EDA. The EDA provides a simpler empirical framework for applying dust attenuation than the dust models in these works. Yet, with its flexibility, we are able to produce optical and UV color-magnitude relations that are in good agreement with observations. Furthermore, with its low computation costs we were able to fully explore our dust parameters.

5.1. *Comparison to Dust Observations*

With our EDA prescription, we are able to accurately reproduce the observed optical and UV color-magnitude relations with our simulations. In addition to reproducing observations, since the EDA assigns dust attenuation curves to each simulated galaxy, we can compare the EDA attenuation curves to dust attenuation measured from observations. We begin with the well-established attenuation-slope relation: star-forming galaxies with higher dust attenuation have shallower attenuation curves. This relation is a consequence of dust scattering dominating absorption at low attenuation while dust absorption dominates at high attenuation (Gordon et al. 1994; Witt & Gordon 2000; Draine 2003; Chevallard et al. 2013). In Figure 8, we present the attenuation-slope relation of star-forming galaxies with SSFR $> 10^{-11}yr^{-1}$ based on the dust attenuation curves predicted by the EDA for
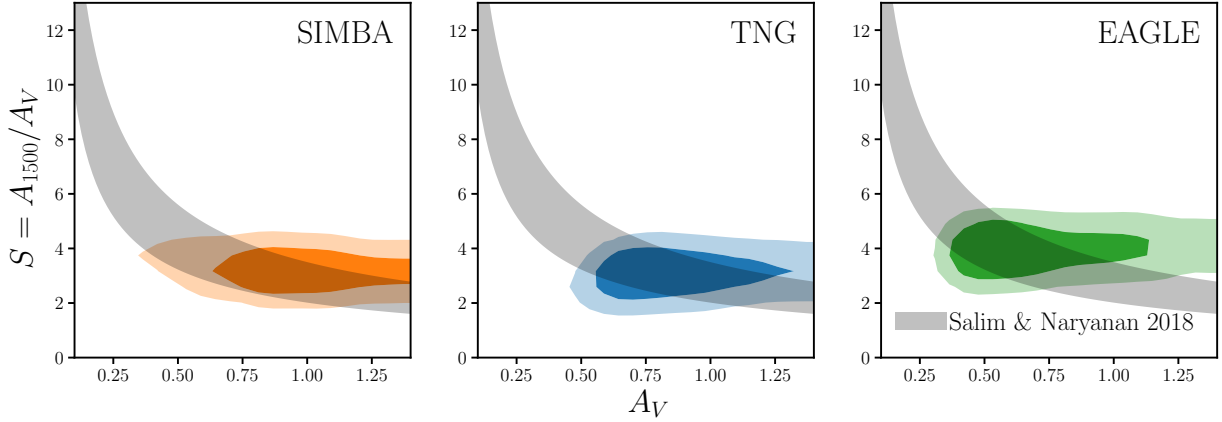
Figure 8. The attenuation-slope relation of star-forming galaxies (SSFR $> 10^{-11} yr^{-1}$), using the attenuation curves predicted by our EDA prescription for the median posterior parameter values of SIMBA (left), TNG (center) and EAGLE (right). For comparison, we include the observed attenuation-slope relation from GSWLC2 (Salim & Narayanan 2020). We use A_V and $S = A(1500\text{Å})/A_V$ as measurements of attenuation and slope, respectively. *The EDA does not predict $A_V < 0.3$ because star-forming galaxies in the simulations are too luminous and require significant attenuation to reproduce observations.* Beyond $A_V > 0.3$, however, there is good agreement between the attenuation-slope relation predicted by the EDA and observations.

the median posteriors of EAGLE (right), TNG (left) and EAGLE (right). For comparison, we include the observed attenuation-slope relations of GSWLC2 galaxies (grey shaded; Salim & Narayanan 2020). For attenuation we use A_V and for slope we use the UV-optical slope, $S = A(1500\text{Å})/A_V$, commonly found in the literature. The contours mark the 68 and 95 percentiles. Most noticably, we find that the EDA does not predict $A_V < 0.3$. This is not due to the selection function imposed by our forward model. The attenuation-slope relation of star-forming galaxies in GSWLC2 does not change significantly if we impose similar selection cuts as our observational sample. Instead, the lack of star-forming galaxies with $A_V < 0.3$ is a consequence of SIMBA, TNG, and EAGLE predicting star-forming galaxies that are more luminous than observations. All of the simulations have star-forming galaxies with intrinsic $M_r < -21$ and $g-r < 0.5$ (Figure 3). This is further corroborated by the $SFR - M*$ relations in Figure 1, where the simulations all have star-forming galaxies with $M_* > 10^{11} M_\odot$, not found in SDSS. To reproduce the SDSS optical color-magnitude relation these galaxies would need to be significantly reddened and attenuated. Hence, any dust prescription for the simulations would require high A_V for star-forming galaxies. Nevertheless, for $A_V > 0.3$, we find good agreement between the attenuation-slope relation predicted by the EDA and observations.

In addition to the attenuation-slope relation, we can also directly compare the attenuation curves predicted by the EDA to measurements from observations for star-forming galaxies. In Figure 9, we present the normalized attenuation curves of star-forming galaxies predicted by the EDA for the median posterior parameter values of SIMBA(orange), TNG (blue), and EAGLE (green). We again define galaxies with SSFR $> 10^{-11} yr^{-1}$ as star-forming. The attenuation curves are normalized at 3000Å and we present the variation in the attenuation curves in the shaded region, 68 percentile. For comparison, we include $A(\lambda)/A(3000\text{Å})$ from the Narayanan et al. (2018) radiative transfer simulation
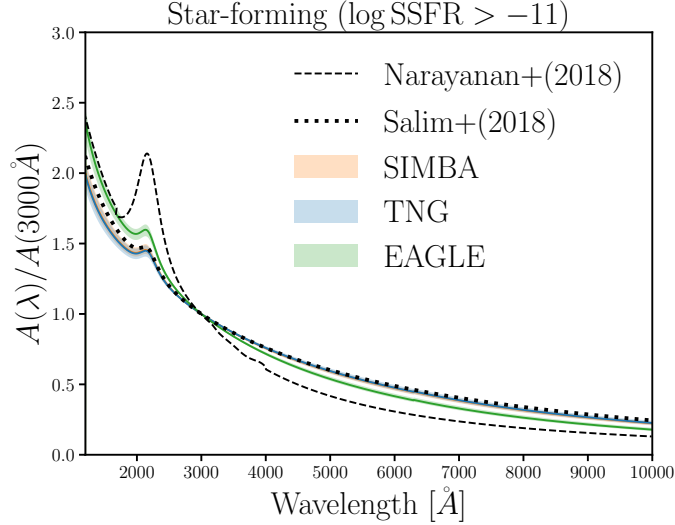
Figure 9. The normalized attenuation curves of star-forming galaxies predicted by the EDA for median posterior parameter values of SIMBA (orange), TNG (blue), and EAGLE (green). Galaxies with $\log \mathrm{SSFR} > -11 \ yr^{-1}$ are classified as star-forming. The attenuation curves are normalized at 3000Å and we mark the 68 percentile of the attenuation curves with the shaded region. For comparison, we include $A(\lambda)/A(3000\text{Å})$ measurements from the Narayanan et al. (2018) radiative transfer simulation (dashed) and Salim et al. (2018) observations (dotted). *The EDA predict attenuation curves of star-forming galaxies that are in good agreement with the attenuation curves measured from the simulation and observations in the literature.*

(dashed) and observations (Salim et al. 2018, dotted). The attenuation curve from Salim et al. (2018) corresponds to star-forming galaxies with $M_* > 10^{10.5} M_\odot$, a similar M_* range as our forward modeled samples. Since we do not vary the UV bump in our EDA prescription, we ignore any discrepancies in the amplitudes of the bump. *Overall, we find good agreement between the EDA attenuation curves for star-forming galaxies and the attenuation curves from observations and simulations in the literature.*

5.2. *The Attenuation Curves of Quiescent Galaxies*

In addition to star-forming galaxies, the EDA also makes predictions on the dust attenuation of quiescent galaxies. This is particularly valuable since dust attenuation in quiescent galaxies is still poorly constrained by observations due to challenges in directly measuring it from observations. For instance, methods that rely on IR luminosities can be contaminated by MIR emission from AGN heating nearby dust (Kirkpatrick et al. 2015). SED fitting methods must also account for AGN MIR emission (Salim et al. 2016; Leja et al. 2018; Salim et al. 2018) and struggle to tightly constrain dust attenuation for quiescent galaxies due to the degeneracies with star formation history and metallicity. With a forward modeling approach, we circumvent these challenges. Instead, we derive the attenuation curves necessary for the simulated quiescent population to reproduce the observed optical and UV photometry.

In Figure 10, we present the attenuation curves of quiescent galaxies predicted by the EDA for the median posterior parameter values of SIMBA (left), TNG (center), and EAGLE (right). Quiescent galaxies are classified using a SSFR $< 10^{-11} yr^{-1}$ cut. Unlike Figure 9, we do not normalize the
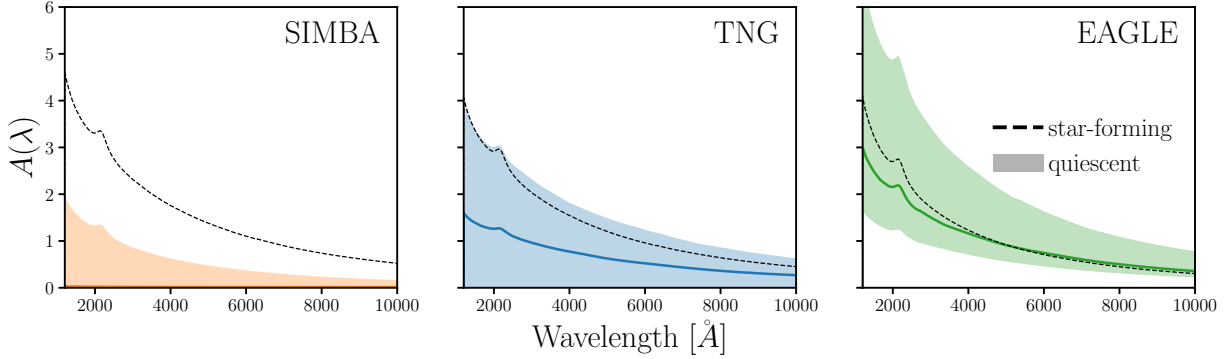
Figure 10. The attenuation curves of quiescent galaxies predicted by the EDA for median posterior parameter values of SIMBA (left), TNG (center), and EAGLE (right). Galaxies with SSFR $< 10^{-11} yr^{-1}$ are classified as quiescent. We mark the 68 percentile of the attenuation curves with the shaded region and include the predicted attenuation curves of star-forming galaxies for comparison (dashed). In all three simulations, *the EDA predicts attenuation curves that have lower amplitudes and shallower slopes than star-forming galaxies.*

attenuation curves at 3000Å. For comparison, we include $A(\lambda)$ of star-forming galaxies predicted by the EDA for the corresponding simulation in each panel (dotted). In all three simulations, quiescent galaxies have attenuation curves with overall lower amplitudes and shallower slopes than star forming galaxies.

We predict $A(\lambda)$ with lower amplitude for quiescent galaxies because quiescent galaxies in SIMBA, TNG, and EAGLE without dust are only slightly more luminous than observations. In the top panels of Figure 3, we see that the most luminous galaxies with the highest $g-r$ color is $< 0.5\ mag$ brighter than the tip of the red sequence in the SDSS color-magnitude relation. For SIMBA+EDA, where we predict $A(\lambda) \sim 0$, the most luminous and optically red galaxies have comparable M_r as the tip of the SDSS red sequence. In contrast, the most luminous blue, star-forming, galaxies are $> 1\ mag$ brighter than the luminous end of the SDSS blue cloud. Despite having lower attenuation than star-forming galaxies, in TNG and EAGLE we predict significant dust attenuation in quiescent galaxies, $A_V > 0.5$. Although this could be a due to shortcomings in TNG and EAGLE in producing quiescent galaxies that are intrinsically too luminous, the prescence of dust attenuation in quiescent galaxies, which is typically neglected, has significant implications. For instance, it strengthens the evidence for the UV upturn phenomenon, the unexpected detections of UV flux in quiescent galaxies (*e.g.* Code 1969; O'Connell 1999; Le Cras et al. 2016; Ali et al. 2018; Dantas et al. 2021). Constraints on the attenuation in quiescent galaxies may also help discern among the different hypotheses: residual star formation activity (*e.g.* Kaviraj et al. 2007), post-main-sequence stellar evolutionary phases (*e.g.* Yi et al. 1997), or binary systems (*e.g.* Han et al. 2007). Since the attenuation curves of quiescent galaxies are difficult to measure from observations, the EDA predictions highlight the advantages of a forward modeling approach and its complementarity with standard approaches.

In Figure 10, we also find that quiescent galaxies have shallower attenuation curves than star-forming galaxies. This is consequence of the fact that SIMBA, TNG, and EAGLE all predict intrinsically UV-red galaxies that do not require significant reddening by dust. This is especially true

for SIMBA and TNG, which predict significant number of galaxies with intrinsic $FUV-NUV > 1$ (Figure 3 and 7). These galaxies are quiescent (SSFR $< 10^{-11} yr^{-1}$) and have high $FUV-NUV$ due to a lack of recent star formation contributing the SED (Leja et al. 2017). When we examine their SFHs, we find that, although they have more star formation than the luminous UV-red galaxies we discuss earlier, they have little star formation in the last 1 Gyr. This implies that SIMBA, whose quiescent galaxies have the shallowest attenuation curve, has the most efficient star-formation quenching among the simulations.

The mass resolution of the simulations can impact the SFHs of quiescent galaxies and, thus, can also impact their observables. The SFHs of simulated galaxies cannot include any star formation below the resolution limit, so the SEDs we compute from them do not include any star formation below the mass resolution. For recent star formation, this can significantly impact on the SED, especially in the FUV and NUV wavelength ranges (Leja et al. 2017). SIMBA, in particular, has a significantly higher mass resolution ($1.82 \times 10^7 M_\odot$) than TNG or EAGLE ($1.4 \times 10^6 M_\odot$, $1.81 \times 10^6 M_\odot$). Fortunately, the quiescent galaxies that pass the M_r and UV selection in our forward model have $M_* \gtrsim 10^{10} M_\odot$ (see Figure 11 later). So the effect of mass resolution on $FUV-NUV$ is $< 0.1\ mag$ for SIMBA and even smaller, $\lesssim 0.01\ mag$, for TNG and EAGLE. Hence, mass resolution does not significantly impact the dust attenuation we predict for quiescent galaxies.

Despite the advantages of our forward modeling approach in deriving dust attenuation curves for quiescent galaxies, we caution readers that we only vary the EDA parameters in this work. The EDA predictions of the quiescent galaxy dust attenuation described in this section assumes that the simulations accurately model the star formation and metallicity histories of quiescent galaxies. Shortcomings in the galaxy formation models, and not the dust attenuation, may be responsible for the intrinsic differences between the quiescent populations in simulations and observations. For instance, we already find in Section 5 that quenching is too efficient in certain SIMBA and TNG quiescent galaxies and results in luminous UV-red galaxies not found in SDSS. TNG and EAGLE may also be producing quiescent galaxies that are overall intrinsically too luminous, which then requires significant dust attenuation to match observations. In principle, however, we can vary both the EDA parameters and the parameters of the galaxy formation models and infer them simultaneously with a foward modeling approach. We will explore this in future work.

5.3. *The Galaxy – Dust Connection*

In the previous section, we presented the attenuation curves predicted by the EDA for quiescent galaxies. By comparing them to the attenuation curves of star-forming galaxies, we found significant SSFR dependence in dust attenuation: quiescent galaxies have attenuation curves with shallower slopes and lower amplitude than star-forming galaxies. With the M_* and SSFR dependent parameterization of our EDA prescription (Eqs 4 and 6), we can examine the connection between the physical properties of the simulated galaxies and dust attenuations in more detail. In Table 2, we list the median values and the 68% confidence interval of the inferred EDA parameter posteriors for the three simulations. In addition to the SSFR dependence from the last section, we also find significant
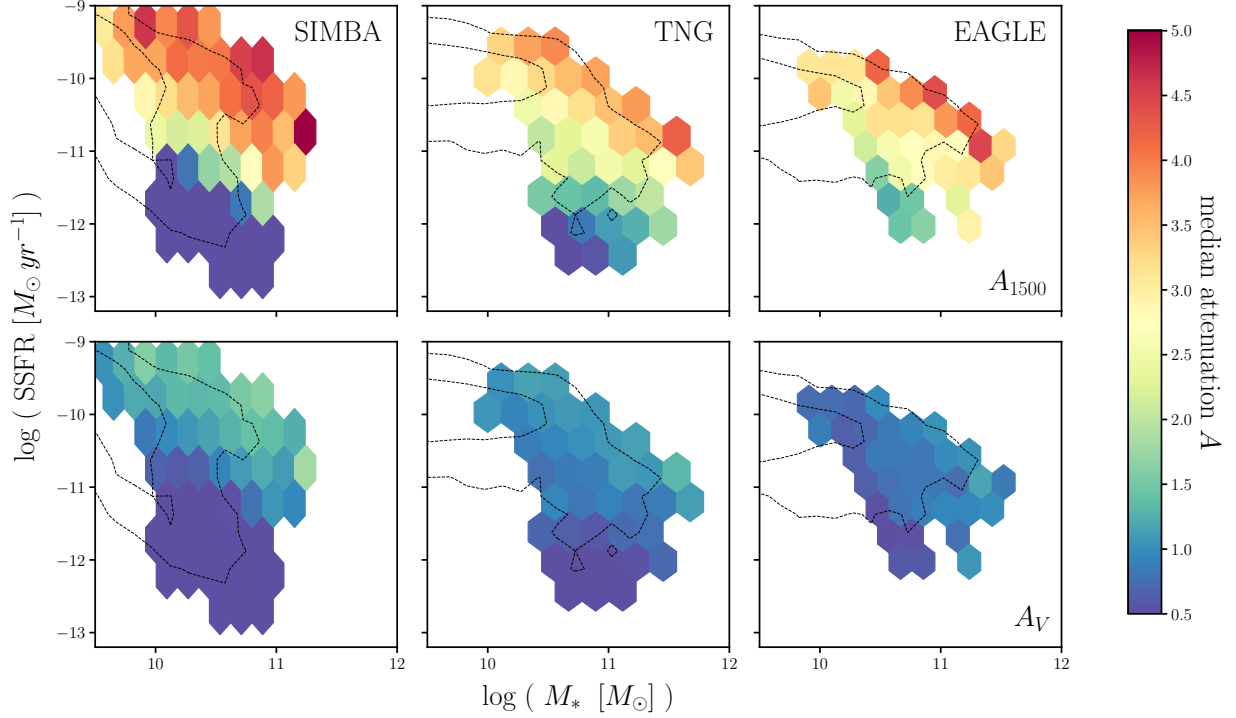
Figure 11. M_* and SSFR dependence of dust attenuation at 1500Å (A_{1500}; top) and at 5500Å (A_V bottom) predicted by the EDA for SIMBA(left), TNG (center), and EAGLE (right). The colormap in each hexbin represents the median attenuation for all simulated galaxies in the bin (right color bar). We only include bins with more than 10 galaxies. For reference, we include in each panel the $M_* - $ SSFR relation of all galaxies from the simulations (black dashed). Overall, simulated galaxies with higher M_* have higher dust attenuation — consistent with the literature. Furthermore, since previous works have primarily focused on star-forming galaxies, the EDA provides new insight into the SSFR dependence of dust attenuation: simulated galaxies with higher SSFR have steeper attenuation curves.

Table 2. Inferred the Empirical Dust Attenuation Model Parameters

	m_{τ, M_*}	$m_{\tau, \text{SSFR}}$	c_τ	m_{δ, M_*}	$m_{\delta, \text{SSFR}}$	c_δ
SIMBA	$1.27^{+0.46}_{-0.46}$	$1.28^{+0.24}_{-0.23}$	$1.58^{+0.12}_{-0.12}$	$0.07^{+0.12}_{-0.12}$	$0.13^{+0.10}_{-0.10}$	$-0.18^{+0.04}_{-0.04}$
TNG	$0.57^{+0.44}_{-0.53}$	$0.62^{+0.21}_{-0.20}$	$1.34^{+0.19}_{-0.21}$	$-0.18^{+0.20}_{-0.19}$	$-0.19^{+0.15}_{-0.16}$	$-0.07^{+0.08}_{-0.08}$
EAGLE	$0.59^{+0.33}_{-0.33}$	$0.18^{+0.20}_{-0.17}$	$0.81^{+0.14}_{-0.15}$	$-0.13^{+0.17}_{-0.18}$	$-0.22^{+0.14}_{-0.14}$	$-0.34^{+0.08}_{-0.08}$

M_* dependence in τ_V: $m_{\tau, M_*} > 0$. V-band dust attenuation is higher for more massive galaxies. There is, however, little M_* dependence in the slope of the dust attenuation.

We take a closer look at the M_* and SSFR dependence of the attenuation curve in Figure 11, where we present dust attenuation at 1500Å (A_{1500}; top) and 5500Å (A_V; bottom) as a function of $\log M_*$ and $\log$ SSFR predicted by the EDA for SIMBA (left), TNG (center) and EAGLE (right). For each hexbin, the colormap represents the median attenuation for all simulated galaxies in the bin.

We only include bins with more than 10 galaxies. We include, for reference, the $M_* -$ SSFR relation of all galaxies in the simulations in black dashed contours.

In each panel, we find that SIMBA, TNG, and EAGLE galaxies with higher M_* have higher dust attenuation — consistent with the literature. Burgarella et al. (2005), for instance, found significant positive M_* dependence in FUV attenuation in NUV-selected and FIR-selected samples. Garn & Best (2010) and Battisti et al. (2016) also find higher attenuation in more massive SDSS star-forming galaxies. Most recently, Salim et al. (2018) find higher V and FUV attenuation for more massive star-forming galaxies in GSWLC2. For the SSFR dependence, we find that galaxies with higher SSFR have higher A_{1500} (top) and A_V (bottom) as well as steeper slopes. We note that the SSFR dependence is not as prominent in EAGLE (see also Table 2). Compared to SIMBA and TNG, EAGLE has a narrower SSFR distribution with no starburst galaxies or quiescent galaxies with SSFR $< 10^{-12} yr^{-1}$. As a result, EAGLE has fewer intrinsically luminous star-forming galaxies or UV red galaxies (Figure 3). This means that EAGLE has a narrower intrinsic $g-r$ and $FUV-NUV$ color distributions that require an overall attenuation and reddenning less dependent on SSFR. Nevertheless, in all simulations, star-forming galaxies have slopes that are consistent with observations (Section 5.1) while quiescent galaxies with the lowest SSFR have nearly flat attenuation curves. Since observations have only focused on star-forming galaxies due to the difficulty in measuring dust attenuation in quiescent galaxies, the EDA predictions provide new insight into the SSFR dependence of dust attenuation. In summary, we find that *SIMBA, TNG, and EAGLE galaxies with higher M_* require overall higher dust attenuation and galaxies with higher* SSFR *require steeper attenuation curves.*

5.4. *Discussion*

We make a number of assumptions and choices in our EDA prescription. First, we use the slab model (Eq. 3) to assign A_V as a function of τ_V and randomly sampled i. This choice is motivated by the fact that the slab model reproduces the correlation between attenuations and inclination found in star-forming galaxies from observations (Conroy 2010; Wild et al. 2011; Battisti et al. 2017; Salim & Narayanan 2020) as well as simulations (*e.g.* Chevallard et al. 2013; Narayanan et al. 2018; Trayford et al. 2020). More importantly, the slab model can reproduce the A_V distribution of SDSS star-forming galaxies as well as the GSWLC2 sample, which includes quiescent galaxies (Appendix A). We therefore conclude that we can sample A_V in our EDA with sufficient flexibility using the slab model.

In our EDA, we also use a parameterization of τ_V and δ that depend linearly on $\log M_*$ and $\log$ SSFR. While the M_* and SSFR dependence of A_V is well-motivated and is found in, for instance, the Salim et al. (2018) GSWLC2 catalog (Appendix A), the linear dependence was chosen primarily for its simplicity. The EDA framework can be easily extended to more flexible parameterizations. Though we already find good agreement with SDSS observations, a more flexible parameterization would likely produce even better agreement with the SDSS color-magnitude relations. The main challenges for a more flexible parameterization would be model selection and finding a well-motivated parameterization.

We demonstrate in this work that accounting for dust attenuation is essential when comparing simulations to observations. After all, none of the simulations reproduce the UV and optical color-magnitude relation without dust (Figure 3). Furthermore, the fact that we can use the EDA to reproduce SDSS observations for different hydrodynamical simulations highlights how our current lack of understanding of dust limits our ability to closely compare galaxy formation models. Our EDA prescription is built on what we currently know about dust attenuation in galaxies: *e.g.* the Noll et al. 2009 parameterization, the UV bump, the slab model, *etc.* Yet with the EDA, simulations that predict galaxy populations with significantly different physical properties (Figure 1) can reproduce the same SDSS observations. For instance, SIMBA has significantly fewer massive galaxies above $M_* > 10^{11} M_\odot$ than TNG or EAGLE (see SMFs in Figure 1). It also has $M_* < 10^{10} M_\odot$ starburst galaxies with SSFR $> 10^{-9.5} yr^{-1}$ (see also Davé et al. 2019 Figures 5 and 6) that are not found in TNG or EAGLE (Figure 11). Despite these differences, the forward modeled color-magnitude relations of SIMBA is able to comparably reproduce SDSS observations, besides the luminous UV red galaxies (Figure 6)

All this suggests that dust is highly degenerate with the differences between simulations. Put another way — if we were to marginalize over dust in our comparison to observations, we would not be able to differentiate between the different galaxy physics prescriptions in the simulations. Hence, current limitations in our understanding of dust is a major bottleneck for investigating galaxy formation using simulations. In the next paper of the series, Starkenburg et al. (in preparation), we will examine whether we can compare the prescriptions for star formation quenching in different galaxy formation models once we include the EDA framework.

Fortunately, there are many avenues for improving our understanding of dust with a forward modeling approach. In this work, we used a restrictive SDSS galaxy sample with a $M_r < -20$, $M_{FUV} < 13.5$, and $M_{NUV} < -14$ completeness limit. Figure 11 illustrates that this selection excludes star-forming galaxies below $M_* \lesssim 10^{10} M_\odot$ and quiescent galaxies below $M_* \lesssim 10^{10.5} M_\odot$. The M_* limit of the selection is lower for SIMBA due to its lack of massive galaxies and low mass starburst galaxies. Instead of imposing this completeness limit, we can include the actual SDSS selection function in the forward model (*e.g.* Dickey et al. 2020). This would allow us to compare the simulations with EDA to the entire SDSS sample, a substantially larger sample with a wider range of galaxies. Upcoming surveys, such as the Bright Galaxy Survey (BGS) of the Dark Energy Spectroscopic Instrument (DESI; DESI~Collaboration et al. 2016; Ruiz-Macias et al. 2020) and galaxy evolution survey of the Prime Focus Spectrograph (PFS; Takada et al. 2014; Tamura et al. 2016), will vastly expand galaxy observations. BGS, for instance, will measure $10\times$ the number of galaxy spectra as SDSS out to $z \sim 0.4$ and with its $r \sim 20$ magnitude limit will probe a significant number of low redshift dwarf galaxies. Such an observational sample will allow us to place tighter constraints on the EDA parameters, which may enable comparisons of the underlying galaxy formation models, and shed light on dust in a broader range of galaxies.

In this work, we also only used observables derived from UV and optical photometry, which means that we have only examined one side of the impact that dust has on galaxy spectra. While dust attenuates light in the optical and UV, it emits light in IR. In fact, even though the simulations
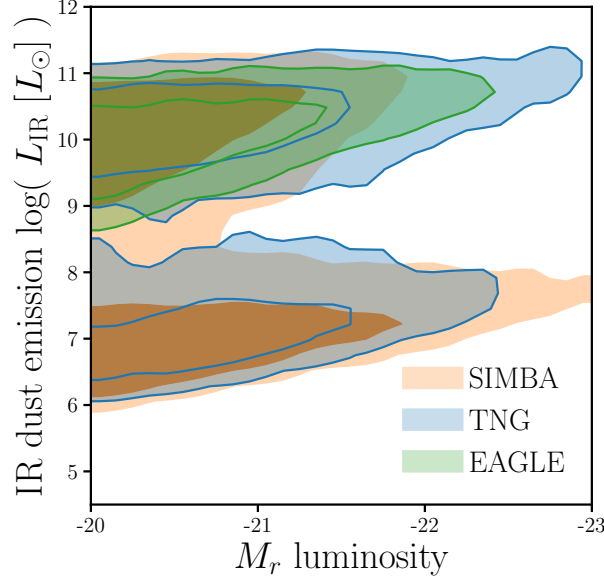
Figure 12. IR dust emission luminosity predicted by the EDA with median parameter values of the SIMBA(orange), TNG (blue), and EAGLE (green) posteriors as a function of M_r. The dust emission is estimated assuming the da Cunha et al. (2008) energy balance. Despite reproducing the same SDSS UV and optical color-magnitude relations, because the simulations require different amounts of dust attenuation to do this, *the EDA predicts significantly different IR dust emissions.* Therefore, including IR observations will significantly improve the constraints on EDA parameters and allow us to better differentiate galaxy formation models.

reproduce the same SDSS UV and optical color-magnitude relations with the EDA, they predict significantly different dust emission in the IR. In Figure 12, we present IR dust emission luminosity, L_{IR}, predicted by the EDA with median parameter values of the EAGLE (orange), TNG (blue), and EAGLE (green) posteriors as a function of the r-band absolute magnitude, M_r. The dust emissions are estimated using the standard energy balance assumption — *i.e.* all starlight attenuated by dust is reemitted in the IR (da Cunha et al. 2008). Most noticeably, SIMBA and TNG have bimodal distributions of dust emission while EAGLE only has luminous IR dust emissions. This is because EAGLE requires significant dust attenuation in all galaxies while SIMBA and TNG require quiescent galaxies to have substantially lower dust attenuation than star-forming galaxies (Figure 10). The luminous mode of the L_{IR} distributions, however, are in good agreement for all simulations, since they all require comparable dust attenuation in star-forming galaxies (Figures 8 and 10). When we compare the IR dust emission of SIMBA+EDA and TNG+EDA further, we find that TNG+EDA produces more luminous galaxies with high IR dust emission ($M_r < -22$ and $L_{rmIR} > 10^9 L_\odot$) since it has more intrinsically luminous star-forming galaxies (Figure 3). On the other hand SIMBA+EDA has more luminous galaxies with fainter IR dust emissions, which correspond to the anomolous luminous UV red galaxies highlighted in Figure 7.

While dust attenuation can be adjusted to reproduce UV and optical observations, since IR dust emission measures the total attenuation, IR observations can place a limit on the total impact of dust

and thereby break the degeneracies between dust and the galaxy physics in simulations. While some upcoming surveys, such as BGS, will have existing near-IR photometry from NEOWISE (Meisner et al. 2018), future observations will dramatically expand the information we have in IR. *Nancy Grace Roman Space Telescope* and *James Webb Space Telescope*, for instance, will provide valuable near and mid-IR observations. Meanwhile, IR observations at even longer wavelengths will came from Atacama Large Millimeter/submillimeter Array or future facilities such as the Next-Generation Very Large Array and Origins Space Telescope.

6. SUMMARY

In this work, we present the EDA, a framework for applying dust attenuation to simulated galaxy populations. It uses a parameterization of the attenuation curves motivated from observations (Noll et al. 2009) and assigns attenuation curves to simulated galaxies based on their physical properties (M_* and SSFR). We apply the EDA to three state-of-the-art hydrodynamical simulations (SIMBA, TNG, and EAGLE) and forward model the optical and UV color-magnitude relations. We then compare the forward modeled simulations to a $M_r < -20, M_{FUV} < -13.5, M_{NUV} < -14.0$ complete SDSS galaxy sample using likelihood-free inference. Based on this comparison, we find the following results:

- Dust attenuation is essential for our hydrodynamical simulations to reproduce observations. Without dust, SIMBA, TNG, and EAGLE all struggle to reproduce the observed UV and optical color-magnitude relation. They predict galaxies that are intrinsically much bluer and more luminous in the optical and with broader distributions of $FUV - NUV$ colors than SDSS.

- With the EDA, each of the simulations are able to produce UV and optical color-magnitude relations in good agreement with SDSS observations. However, we find that star formation quenching is too efficient for some of the most massive quiescent galaxies in SIMBA and TNG. When forward modeled, these galaxies appear as luminous UV red galaxies outside the observed UV color-magnitude relation that cannot be reconciled by dust.

- The attenuation curves of star-forming galaxies predicted by the EDA for the simulations are in good agreement with the observed attenuation-slope relation. They also closely reproduce the observed attenuation curves of star-forming galaxies. The simulations, however, predict star-forming galaxies that are intrinsically more luminous than observations. Hence, the EDA does not predict star-forming galaxies with $A_V < 0.3$, found in the literature.

- Lastly, with the EDA we predict the attuenation curves of quiescent galaxies, which observations struggle to directly measure. We find that quiescent galaxies have $A(\lambda)$ curves with lower amplitudes and shallower slopes than star-forming galaxies. Over the entire population, we find that more massive galaxies have higher overall dust attenuation while galaxies with higher SSFR have steeper attenuation curves.

Our results clearly demonstrate that the EDA and a forward modeling approach provides key insights into dust attenuation. For those uninterested in dust, the EDA also provides a computationally

feasible framework for marginalizing over dust when comparing simulations to observations. However, we find that dust attenuation is *highly* degenerate with differences in their galaxy physics prescriptions. Even though the simulations predict galaxy populations with significantly different physical properties, there is enough uncertainty in our understanding of dust that by adjusting attenuation alone they can all reproduce the same SDSS observations. This also suggests that any comparisons across simulations must marginalize over dust attenuation or run the risk of overinterpretation. Therefore, our current understanding of dust, or lack of, limit our ability to distinguish between the various hydrodynamical models and is a major bottleneck for investigating galaxy formation using simulations.

The forward modeling approach we present offers many avenues for improving on our understanding of dust. In this paper, we used a restrictive M_r complete SDSS galaxy sample. Comparison to a larger observed galaxy sample will place tighter constraints on EDA parameters and enable better differentiation between the simulations. One way to expand the observed galaxy sample would be to remove the completeness limits and include the SDSS survey selection function to our forward model. Upcoming surveys, such as the DESI Bright Galaxy Survey and the PFS Galaxy Evolution Survey, will also soon provide much larger observational galaxy samples. Furthermore, IR observations, which measure dust emission and trace the total dust attenuation, also have the potential to tightly constrain the EDA parameters and therefore break degeneracies between dust and the galaxy physics in simulations. In the next paper of the series, we will use the forward modeling approach with the EDA to investigate star formation quenching in galaxy formation models. In other future works, we will apply the EDA and a forward modeling approach to more statistically powerful samples and include IR observables in order to tightly constrain and reveal new insights into dust attenuation.
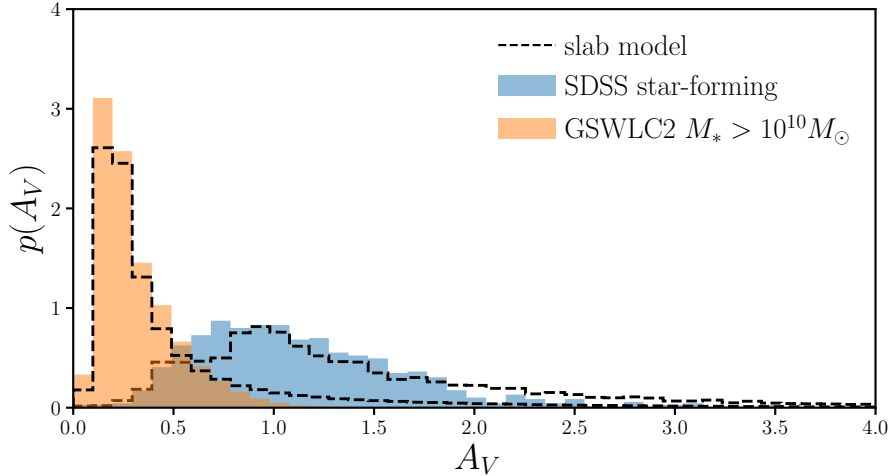
Figure 13. The A_V distributions, $p(A_V)$, generated from the slab model (Eq. 3; black dash) compared to $p(A_V)$ of star-forming galaxies in SDSS (blue) and of $M_* > 10^{10} M_\odot$ galaxies in the Salim et al. (2018) GSWLC2 sample (orange). The A_V values for both observations are derived using SED fitting (Brinchmann et al. 2004; Salim et al. 2018). Meanwhile, for the slab model, we generate A_V values for each galaxy in the SDSS and GSWLC2 samples using Eq. 3 with its measured M_* and SSFR. The significant difference between the $p(A_V)$ of SDSS and GSWLC2 is due to inconsistencies in the A_V measurements of the two catalogs. It illustrates the challenges in observationally measuring A_V and, again, highlights the advantages of our forward modeling approach. Despite the significant differences between the two, the slab model is able to generate $p(A_V)$ in good agreement with $p(A_V)$ from both observations with parameter values chosen within the Table 1 prior range. Therefore, the slab model provides a sufficiently flexible prescription for our EDA.

APPENDIX

A. THE SLAB MODEL BASED EDA

In our EDA prescription, we use the slab model to determine A_V, the amplitude of attenuation, as a function of a randomly sampled inclination, i, and τ_V (see Eq. 3 in Section 3). The slab model is based on the assumption that dust in galaxies have slab-like geometry and illuminated by the stellar radiation source (Somerville & Primack 1999). For a given τ_V, the attenuation depends solely on the orientation of the galaxy. While this simplification reproduces the correlation between A_V and i found in observed star-forming galaxies (*e.g.* Conroy et al. 2010; Wild et al. 2011; Battisti et al. 2017; Salim & Narayanan 2020), it ignores the detailed star-to-dust geometry that impacts

the attenuation curve. It also does not provide a well-motivated prescription for quiescent galaxies, which typically have elliptical morphologies. Despite its limitations, the slab model provides a robust empirical prescription that allows us to produce realistic distributions of A_V.

In Figure 13, we compare the A_V distributions, $p(A_V)$, of star-forming galaxies in SDSS (blue) and galaxies in the Salim et al. (2018) GSWLC2 sample (orange) to the $p(A_V)$ generated from the slab model (black dashed). The A_V values of the SDSS are derived using SED fitting from the Brinchmann et al. (2004) MPA-JHU catalog. The A_V values of the GSWLC2 galaxies are also derived from SED fitting UV and optical photometry from GALEX and SDSS observations as well as mid-IR photometry from WISE. We include all GSWLC2 galaxies, including quiescent galaxies, above $M_* > 10^{10} M_\odot$. We generate two $p(A_V)$ with the slab model for the SDSS and GSWLC2 samples separately. For each SDSS/GSWLC2 galaxy, we determine A_V by uniformly sampling $\cos i$ from 0 to 1 and derive τ_V (Eq. 4) with the galaxy's measured M_* and SSFR. We pick $m_{\tau,M_*}, m_{\tau,\mathrm{SSFR}}, c_\tau$ values within the prior range (Table 1) by hand to roughly reproduce the SDSS and GSWLC2 $p(A_V)$ distributions.

Galaxies in SDSS and GSWLC2 have substantially different $p(A_V)$. This is due to inconsistencies in the A_V measurements of MPA-JHU and GSWLC2 — even for the same galaxy, the A_V measurements from the two catalogs differ significantly. This difference in $p(A_V)$ illustrates the challenges in directly measuring dust attenuation and yet again highlights the advantages of our forward modeling approach. Despite the dramatic differences between the two, the slab model can produce $p(A_V)$ in good agreement with both observed distributions. We therefore conclude that the slab model provides a sufficiently flexible prescription to sample a realistic distribution of A_V.

In addition to the slab model, in the EDA, we also use a linear dependence on M_* and SSFR in the V band optical depth, τ_V (see Eq. 4). This parameterization is motivated by observations that find significant correlation between A_V and M_* and SSFR (e.g. Garn & Best 2010; Battisti et al. 2016; Salim & Narayanan 2020). We take a closer look at this correlation using the GWSLC2 sample in Figure 14. We present the dependence of A_V on M_* (left panel) and SSFR (right panel). In the left panel, we divide the GSWLC2 galaxies by SSFR: SSFR $< 10^{-11} yr^{-1}$ (purple), $10^{-11} <$ SSFR $< 10^{-10} yr^{-1}$ (red), and $10^{-10} <$ SSFR (orange). For each of the SSFR bins, we find significant $\log M_*$ dependence in A_V: galaxies with higher SSFR have a stronger M_* dependence. In the right, we divide the galaxies by M_*: $10^{9.5} < M_* < 10^{10.5} M_\odot$ (blue) and $10^{10.5} M_\odot < M_*$ (green). Although both M_* bins have some SSFR dependence, the dependence is stronger for galaxies with $M_* > 10^{10.5} M_\odot$. This stellar mass limit roughly corresponds to galaxies that are included in our forward model (see Figure 11). The M_* and SSFR dependence we find in A_V from the GSWLC2 sample is consistent with previous observations and further motivates our EDA prescription.

REFERENCES

Abazajian K. N., et al., 2009, The Astrophysical Journal Supplement Series, 182, 543

Aihara H., et al., 2011, The Astrophysical Journal Supplement Series, 193, 29

Akeret J., Refregier A., Amara A., Seehars S., Hasner C., 2015, Journal of Cosmology and Astroparticle Physics, 2015, 043
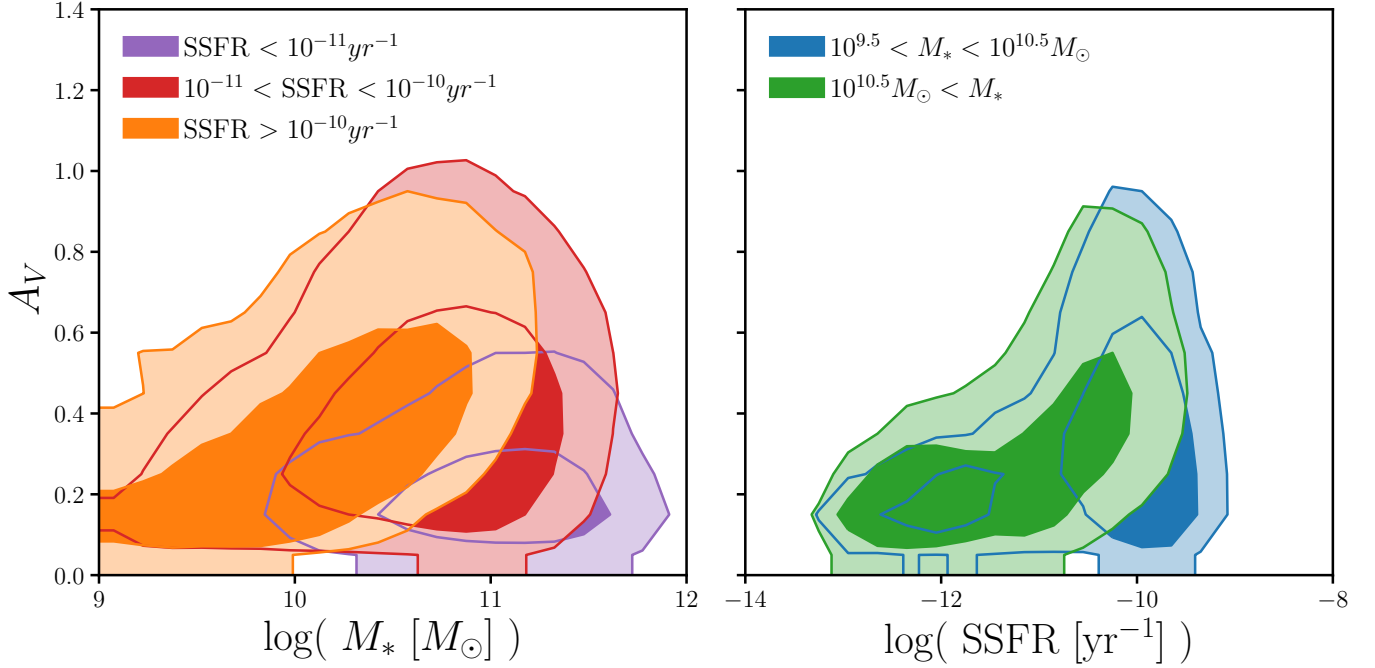
Figure 14. Dependence of A_V on M_* (left) and SSFR (right) for the Salim et al. (2018) GSWLC2 sample. In the left panel, we divide the GSWLC2 sample into bins of SSFR: SSFR $< 10^{-11}yr^{-1}$ (purple), $10^{-11} <$ SSFR $< 10^{-10}yr^{-1}$ (red), and $10^{-10} <$ SSFR (orange). In each of the SSFR bins, we find significant M_* dependence. In the right panel, we divide the sample into bins of M_*: $10^{9.5} < M_* < 10^{10.5}M_\odot$ (blue) and $10^{10.5}M_\odot < M_*$ (green). In the $M_* > 10^{10.5}M_\odot$ bin, which roughly corresponds to our SDSS sample, we find significant SSFR dependence. The M_* and SSFR dependence in A_V we find in GSWLC2 is consistent with previous works and provides further motivation for our EDA prescription.

Ali S. S., Bremer M. N., Phillipps S., De Propris R., 2018, Monthly Notices of the Royal Astronomical Society, 476, 1010

Alsing J., Wandelt B., Feeney S., 2018, arXiv:1801.01497 [astro-ph]

Anglés-Alcázar D., Davé R., Faucher-Giguère C.-A., Özel F., Hopkins P. F., 2017, Monthly Notices of the Royal Astronomical Society, 464, 2840

Baes M., Trčka A., Camps P., Nersesian A., Trayford J., Theuns T., Dobbels W., 2019, arXiv:1901.08878 [astro-ph]

Battisti A. J., Calzetti D., Chary R.-R., 2016, The Astrophysical Journal, 818, 13

Battisti A. J., Calzetti D., Chary R.-R., 2017, The Astrophysical Journal, 840, 109

Beaumont M. A., Cornuet J.-M., Marin J.-M., Robert C. P., 2009, Biometrika, 96, 983

Blanton M. R., Roweis S., 2007, The Astronomical Journal, 133, 734

Blanton M. R., et al., 2005, The Astronomical Journal, 129, 2562

Blanton M. R., Kazin E., Muna D., Weaver B. A., Price-Whelan A., 2011, The Astronomical Journal, 142, 31

Booth C. M., Schaye J., 2009, Monthly Notices of the Royal Astronomical Society, 398, 53

Brinchmann J., Charlot S., White S. D. M., Tremonti C., Kauffmann G., Heckman T., Brinkmann J., 2004, Monthly Notices of the Royal Astronomical Society, 351, 1151

Burgarella D., Buat V., Iglesias-Páramo J., 2005, Monthly Notices of the Royal Astronomical Society, 360, 1413

Calzetti D., 2001, New Astronomy Reviews, 45, 601

Cameron E., Pettitt A. N., 2012, Monthly Notices of the Royal Astronomical Society, 425, 44

Camps P., Baes M., 2015, Astronomy and Computing, 9, 20

32

Carnall A. C., Leja J., Johnson B. D., McLure R. J., Dunlop J. S., Conroy C., 2018, arXiv:1811.03635 [astro-ph]

Chabrier G., 2003, Publications of the Astronomical Society of the Pacific, 115, 763

Chevallard J., Charlot S., Wandelt B., Wild V., 2013, Monthly Notices of the Royal Astronomical Society, 432, 2061

Choi J., Dotter A., Conroy C., Cantiello M., Paxton B., Johnson B. D., 2016, ApJ, 823, 102

Code A. D., 1969, Publications of the Astronomical Society of the Pacific, 81, 475

Conroy C., 2010, Monthly Notices of the Royal Astronomical Society, 404, 247

Conroy C., 2013, Annual Review of Astronomy and Astrophysics, 51, 393

Conroy C., Gunn J. E., White M., 2009, The Astrophysical Journal, 699, 486

Conroy C., White M., Gunn J. E., 2010, The Astrophysical Journal, 708, 58

Crain R. A., et al., 2015, Monthly Notices of the Royal Astronomical Society, 450, 1937

DESI~Collaboration et al., 2016, arXiv:1611.00036 [astro-ph]

Dalla Vecchia C., Schaye J., 2012, Monthly Notices of the Royal Astronomical Society, 426, 140

Dantas M. L. L., Coelho P. R. T., Sánchez-Blázquez P., 2021, Monthly Notices of the Royal Astronomical Society, 500, 1870

Davé R., Thompson R., Hopkins P. F., 2016, Monthly Notices of the Royal Astronomical Society, 462, 3265

Davé R., Rafieferantsoa M. H., Thompson R. J., 2017a, arXiv:1704.01135 [astro-ph]

Davé R., Rafieferantsoa M. H., Thompson R. J., Hopkins P. F., 2017b, Monthly Notices of the Royal Astronomical Society, 467, 115

Davé R., Anglés-Alcázar D., Narayanan D., Li Q., Rafieferantsoa M. H., Appleby S., 2019, Monthly Notices of the Royal Astronomical Society, 486, 2827

Davé R., Crain R. A., Stevens A. R. H., Narayanan D., Saintonge A., Catinella B., Cortese L., 2020, MNRAS, 497, 146

Del Moral P., Doucet A., Jasra A., 2012, Statistics and Computing, 22, 1009

Dickey C. M., et al., 2020, arXiv e-prints, 2010, arXiv:2010.01132

Diggle P. J., Gratton R. J., 1984, Journal of the Royal Statistical Society. Series B (Methodological), 46, 193

Dotter A., 2016, ApJS, 222, 8

Draine B. T., 2003, The Astrophysical Journal, 598, 1017

Fontanot F., Somerville R. S., Silva L., Monaco P., Skibba R., 2009, Monthly Notices of the Royal Astronomical Society, 392, 553

Galliano F., Galametz M., Jones A. P., 2018, Annual Review of Astronomy and Astrophysics, 56, 673

Garn T., Best P. N., 2010, Monthly Notices of the Royal Astronomical Society, 409, 421

Genel S., et al., 2014, Monthly Notices of the Royal Astronomical Society, 445, 175

Gonzalez-Perez V., Lacey C. G., Baugh C. M., Frenk C. S., Wilkins S. M., 2013, Monthly Notices of the Royal Astronomical Society, 429, 1609

Gordon K. D., Witt A. N., Carruthers G. R., Christensen S. A., Dohne B. C., 1994, The Astrophysical Journal, 432, 641

Granato G. L., Lacey C. G., Silva L., Bressan A., Baugh C. M., Cole S., Frenk C. S., 2000, The Astrophysical Journal, 542, 710

Hahn C., Vakili M., Walsh K., Hearin A. P., Hogg D. W., Campbell D., 2017a, Monthly Notices of the Royal Astronomical Society, 469, 2791

Hahn C., Tinker J. L., Wetzel A. R., 2017b, The Astrophysical Journal, 841, 6

Hahn C., Tinker J. L., Wetzel A., 2019a, arXiv:1910.01644 [astro-ph]

Hahn C., Beutler F., Sinha M., Berlind A., Ho S., Hogg D. W., 2019b, Monthly Notices of the Royal Astronomical Society, 485, 2956

Hahn C., et al., 2019c, The Astrophysical Journal, 872, 160

Han Z., Podsiadlowski P., Lynas-Gray A. E., 2007, Monthly Notices of the Royal Astronomical Society, 380, 1098

Hayward C. C., Smith D. J. B., 2015, Monthly Notices of the Royal Astronomical Society, 446, 1512

Hopkins P. F., 2015, Monthly Notices of the Royal Astronomical Society, 450, 53

Hopkins P. F., et al., 2017, arXiv:1707.07010 [astro-ph]

Hou K.-C., Hirashita H., Nagamine K., Aoyama S., Shimizu I., 2017, Monthly Notices of the Royal Astronomical Society, 469, 870

Ishida E. E. O., et al., 2015, Astronomy and Computing, 13, 1

Jonsson P., 2006, Monthly Notices of the Royal Astronomical Society, 372, 2

Katsianis A., et al., 2020, Monthly Notices of the Royal Astronomical Society, 492, 5592

Kaviraj S., et al., 2007, The Astrophysical Journal Supplement Series, 173, 619

Kirkpatrick A., Pope A., Sajina A., Roebuck E., Yan L., Armus L., Díaz-Santos T., Stierwalt S., 2015, The Astrophysical Journal, 814, 9

Kriek M., Conroy C., 2013, The Astrophysical Journal Letters, 775, L16

Le Cras C., Maraston C., Thomas D., York D. G., 2016, Monthly Notices of the Royal Astronomical Society, 461, 766

Leja J., Johnson B. D., Conroy C., van Dokkum P. G., Byler N., 2017, The Astrophysical Journal, 837, 170

Leja J., Johnson B. D., Conroy C., van Dokkum P., 2018, The Astrophysical Journal, 854, 62

Leja J., Carnall A. C., Johnson B. D., Conroy C., Speagle J. S., 2019, ApJ, 876, 3

Lin C.-A., Kilbinger M., Pires S., 2016, Astronomy and Astrophysics, 593, A88

McAlpine S., et al., 2016, Astronomy and Computing, 15, 72

Meisner A. M., Lang D., Schlegel D. J., 2018, Research Notes of the American Astronomical Society, 2, 1

Narayanan D., Conroy C., Davé R., Johnson B. D., Popping G., 2018, The Astrophysical Journal, 869, 70

Natale G., Popescu C. C., Tuffs R. J., Debattista V. P., Fischera J., Grootes M. W., 2015, Monthly Notices of the Royal Astronomical Society, 449, 243

Nelson D., et al., 2015, Astronomy and Computing, 13, 12

Nelson D., et al., 2018, Monthly Notices of the Royal Astronomical Society, 475, 624

Noll S., Burgarella D., Giovannoli E., Buat V., Marcillac D., Muñoz-Mateos J. C., 2009, Astronomy and Astrophysics, 507, 1793

O'Connell R. W., 1999, Annual Review of Astronomy and Astrophysics, 37, 603

Paxton B., Bildsten L., Dotter A., Herwig F., Lesaffre P., Timmes F., 2011, ApJS, 192, 3

Paxton B., et al., 2013, ApJS, 208, 4

Paxton B., et al., 2015, ApJS, 220, 15

Pillepich A., et al., 2018, Monthly Notices of the Royal Astronomical Society, 473, 4077

Popping G., Somerville R. S., Galametz M., 2017, Monthly Notices of the Royal Astronomical Society, 471, 3152

Pritchard J. K., Seielstad M. T., Perez-Lezaun A., Feldman M. W., 1999, Molecular Biology and Evolution, 16, 1791

Reddy N. A., et al., 2015, The Astrophysical Journal, 806, 259

Rocha M., Jonsson P., Primack J. R., Cox T. J., 2008, Monthly Notices of the Royal Astronomical Society, 383, 1281

Ruiz-Macias O., et al., 2020, arXiv:2007.14950 [astro-ph]

Salim S., Narayanan D., 2020, arXiv:2001.03181 [astro-ph]

Salim S., et al., 2016, The Astrophysical Journal Supplement Series, 227, 2

Salim S., Boquien M., Lee J. C., 2018, The Astrophysical Journal, 859, 11

Sánchez-Blázquez P., et al., 2006, MNRAS, 371, 703

Schaye J., et al., 2015, Monthly Notices of the Royal Astronomical Society, 446, 521

Seon K.-I., Draine B. T., 2016, The Astrophysical Journal, 833, 201

Somerville R. S., Primack J. R., 1999, Monthly Notices of the Royal Astronomical Society, 310, 1087

Somerville R. S., Gilmore R. C., Primack J. R., Domínguez A., 2012, Monthly Notices of the Royal Astronomical Society, 423, 1992

Speagle J. S., Steinhardt C. L., Capak P. L., Silverman J. D., 2014, The Astrophysical Journal Supplement Series, 214, 15

Springel V., 2005, Monthly Notices of the Royal Astronomical Society, 364, 1105

Springel V., et al., 2018, Monthly Notices of the Royal Astronomical Society, 475, 676

Steinacker J., Baes M., Gordon K. D., 2013, Annual Review of Astronomy and Astrophysics, 51, 63

Takada M., et al., 2014, Publications of the Astronomical Society of Japan, 66, R1

34

Tamura N., et al., 2016, in Ground-Based and Airborne Instrumentation for Astronomy VI. eprint: arXiv:1608.01075, p. 99081M, doi:10.1117/12.2232103

Tavare S., Balding D. J., Griffiths R. C., Donnelly P., 1997, Genetics, 145, 505

Tinker J., Wetzel A., Conroy C., 2011, preprint, 1107, arXiv:1107.5046

Trayford J. W., et al., 2015, Monthly Notices of the Royal Astronomical Society, 452, 2879

Trayford J. W., et al., 2017, Monthly Notices of the Royal Astronomical Society, 470, 771

Trayford J. W., Lagos C. d. P., Robotham A. S. G., Obreschkow D., 2020, Monthly Notices of the Royal Astronomical Society, 491, 3937

Tress M., et al., 2018, Monthly Notices of the Royal Astronomical Society, 475, 2363

Vogelsberger M., et al., 2014, Monthly Notices of the Royal Astronomical Society, 444, 1518

Vogelsberger M., et al., 2020, Monthly Notices of the Royal Astronomical Society, 492, 5167

Walcher J., Groves B., Budavári T., Dale D., 2011, Astrophysics and Space Science, 331, 1

Wechsler R. H., Tinker J. L., 2018, preprint, 1804, arXiv:1804.03097

Weinberger R., et al., 2018, Monthly Notices of the Royal Astronomical Society, 479, 4056

Weyant A., Schafer C., Wood-Vasey W. M., 2013, The Astrophysical Journal, 764, 116

Wild V., Charlot S., Brinchmann J., Heckman T., Vince O., Pacifici C., Chevallard J., 2011, Monthly Notices of the Royal Astronomical Society, 417, 1760

Wilkins S. M., Gonzalez-Perez V., Lacey C. G., Baugh C. M., 2012, Monthly Notices of the Royal Astronomical Society, 424, 1522

Witt A. N., Gordon K. D., 1996, The Astrophysical Journal, 463, 681

Witt A. N., Gordon K. D., 2000, The Astrophysical Journal, 528, 799

Yi S., Demarque P., Kim Y.-C., 1997, The Astrophysical Journal, 482, 677

Yung L. Y. A., Somerville R. S., Finkelstein S. L., Popping G., Davé R., 2019, Monthly Notices of the Royal Astronomical Society, 483, 2983

da Cunha E., Charlot S., Elbaz D., 2008, Monthly Notices of the Royal Astronomical Society, 388, 1595